Two-Dimensional Crystallography of Amphiphilic Molecules at the Air–Water Interface

By Didier Jacquemain, Sharon Grayer Wolf, Franck Leveiller, Moshe Deutsch, Kristian Kjaer,* Jens Als-Nielsen,* Meir Lahav,* and Leslie Leiserowitz*

The advent of well-collimated, high-intensity synchrotron X-ray sources and the consequent development of surface-specific X-ray diffraction and fluorescence techniques have recently revolutionized the study of Langmuir monolayers at the air–liquid interface. These methods allowed for the first time the determination of the in-plane and vertical structure of such monolayers with a resolution approaching the atomic level. We briefly describe these methods, including grazing incidence X-ray diffraction, specular reflectivity, Bragg rods, standing waves, and surface fluorescence techniques, and review recent results obtained from them for Langmuir films. The methods have been successfully applied in the elucidation of the structure of crystalline aggregates of amphiphilic molecules such as alcohols, carboxylic acids and their salts, α-amino acids, and phospholipids at the water surface. In addition, it became possible to monitor by diffraction the growth and dissolution of the crystalline self-aggregates as well as structural changes occurring by phase transitions. Furthermore, the surface X-ray methods shed new light on the structure of the underlying ionic layer of attached solvent or solute species. Examples are given where singly or doubly charged ions bound to the two-dimensional (2D) crystal form either an ordered or diffuse counterionic layer. Finally, the surface diffraction methods provide data on transfer of structural information from 2D clusters to 3D single crystals, which had been successfully accomplished by epitaxial-like crystallization both in organic and inorganic crystals.

1. Introduction

Early in the century, Langmuir demonstrated in a series of elegant experiments that amphiphilic molecules composed of a hydrophobic tail and a hydrophilic head group accumulate at the air–water interface.[1] These films still elicit wide interest because of their importance in the pure and applied sciences. For instance, Langmuir monolayers serve as useful models for elucidating structure and function of biological membranes in their interactions with lipids, steroids, sugars, proteins, and ions.[2] They may also be designed to induce nucleation of organic or inorganic three-dimensional (3D) crystals from molecules or ions present in the subphase by a form of epitaxial growth.[3] In this respect they may be used as models for the study of biological mineralization which involves the use of two-dimensional (2D) surfaces of biological macromolecules to induce the mineral crystallization.[4] The design of monolayers with interfaces which mimic the surfaces of 3D crystals also provides a means of examining crystal surface–solvent interactions in order to understand the effect of the solvent on crystal growth. Furthermore, a knowledge of the characteristics of compressed and uncompressed Langmuir monolayers of water-insoluble amphiphiles should help to unravel the packing characteristics at the air–water interface of water-soluble amphiphiles, where even less is known about their 2D arrangements.[5] In addition Langmuir films are easily transferred to solid supports for the formation of multilayer (Langmuir–Blodgett) films,[6] for potential use as piezoelectric sensors,[7] soft X-ray monochromators, nonlinear optical devices,[8] and in molecular electronics.[9]

Despite the widespread interest in Langmuir films, many of the methods used to characterize their properties do not give direct information on their crystalline packing arrangements. These methods include measurements of surface pressure versus average molecular area,[10] surface potential data,[10] nonlinear optics from surfaces,[11] and IR spectroscopy.[12] Epifluorescence microscopy does furnish some information on crystallinity and morphology on the micron level, but is limited to films of dyes or films containing dye probes.[13] Thus, knowledge on the molecular level of two-dimensional monolayers has been achieved, in the main, from three-dimensional crystals. Indeed, M. Lundquist wrote[14] in a review from 1978: "...there still remains much to be learned especially about the detailed structure of condensed monolayers and regarding the mechanism of molecular rearrangement in monolayer phase transitions. As there are no methods available for direct structure analysis of a monolayer on a water substrate, knowledge of the monolayer structure has, for the most part, been achieved by a sort of translation and application of the knowledge gained from the study of the ordinary three-dimensional state." Only recently, with the advent of intense and well-collimated X-ray beams of variable wavelength from synchrotron sources, has it became possible to obtain direct structural information on the packing of these films by X-ray surface methods.

Here we shall describe some of these new techniques, the information they provide, and review some of the structural results obtained. Emphasis will be placed on monolayer packing arrangements, particularly in terms of the polar head

[*] Dr. M. Lahav, Dr. L. Leiserowitz, D. Jacquemain, Dr. S. Grayer Wolf, F. Leveiller
Department of Materials and Interfaces
Weizmann Institute of Science
Rehovot 76100 (Israel)
Dr. M. Deutsch
Physics Department, Bar-Ilan University
Ramat-Gan 52100 (Israel)
Dr. K. Kjaer, Dr. J. Als-Nielsen
Physics Department, Risø National Laboratory
DK 4000 Roskilde (Denmark)

  0570-0833/92/0202-0130 $ 3.50+.25/0

groups. We shall examine self-aggregation, growth and domain size of 2D crystallites, surface pressure- and temperature-driven phase transitions, and the effect of pH, ions and solute molecules in the aqueous subphase on molecular packing and crystallinity. We shall discuss the role played by electrostatic interactions and structural complementarity in the induction of 3D crystal nucleation at the monolayer–solution interface.

The results obtained so far already necessitate a revision of our basic concepts on properties such as crystallinity, phase assignment, and diffuse and nondiffuse counterionic layers.

2. Surface Sensitive X-ray Methods

The intensity measured in a conventional X-ray scattering experiment is proportional to the number of scatterers, i.e., the irradiated sample volume. This, in turn, is proportional to the penetration depth of the radiation in a sample. For X-rays of about 1 Å wavelength, this penetration ranges from a few micrometers for highly absorbing material to a few millimeters for low absorbing materials. By contrast, the depth to which surface effects persist rarely extends beyond 100 Å. Consequently, scattering from the surface region is so weak compared to that from the bulk that it is completely swamped. A method restricting the penetration depth to the surface region is therefore a prerequisite for all surface diffraction/scattering experiments. This can be achieved by using grazing angles of incidence and employing the phenomenon of total external reflection from the surface.

The refractive index n of matter for X-rays in the 1 Å wavelength range is given by Equation (1),[15] where $\delta = 2\pi\rho r_0/k^2$ ($k = 2\pi/\lambda$ is the X-ray wavenumber and λ is the wavelength). ρ is the electron density and $r_0 = 2.82 \times 10^{-13}$ cm is the classical electron radius. Typically δ is of the order of 10^{-5}. The term β is equal to $-\mu/(2k)$ where μ is the linear absorption coefficient. For X-rays of wavelength $\lambda \approx 1$ Å, absorption is small and $\beta \ll \delta$.

$$n = 1 - \delta - i\beta \tag{1}$$

Consider now a plane wave with wavevector $\boldsymbol{k}_i$ incident at an angle α_i on a planar interface separating a homogeneous medium from the vacuum, as shown in Figure 1. The wave will be partially reflected into the vacuum in the direction given by $\alpha_r = \alpha_i$ and partially refracted into the lower medium in the direction given by α_r'. Snell's law for this case yields Equation (2).

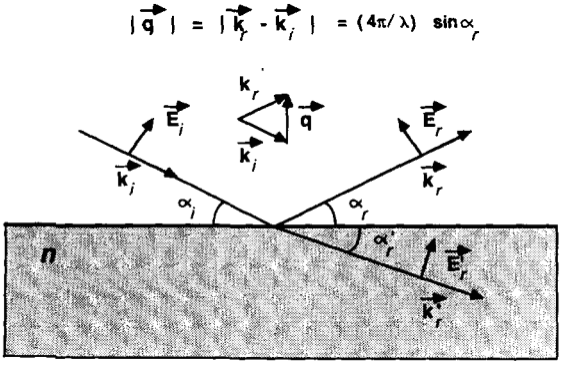

Fig. 1. Refracted (E_r') and reflected (E_r) waves resulting from an incident plane wave with amplitude $|E_i|$ upon an interface between air and a material of refractive index n. Electric fields E are illustrated for one polarization only. The symbol q is the scattering vector, with k_i and k_r the incident and reflected wave vectors of magnitude $2\pi/\lambda$. Note that for $n \lesssim 1$, $\alpha_r' < \alpha_i = \alpha_r$. This provides for total reflection at angles $\alpha_r < \alpha_c$, where α_c is the critical angle for total external reflection.

$$n \cos \alpha_r' = \cos \alpha_i \tag{2}$$

As $n < 1$, for angles of incidence α_i less than or equal to an angle α_c, which is defined as $\alpha_c = \cos^{-1}(n) = (2\delta)^{1/2}$, the well-known phenomenon of total reflection occurs:[16] the incident wave is totally reflected, while the refracted wave becomes evanescent traveling along the surface. The amplitude of the evanescent wave decays exponentially with depth. Figure 2 shows the penetration depth Λ of the X-rays in water versus angle of incidence α_i. For $\alpha_i < 0.5\alpha_c$, the penetration depth is 46 Å independent of the X-ray wavelength. The evanescent wave may therefore be diffracted by crystalline material in a surface layer of that thickness and provides information on its in-plane structure. Such diffraction is called grazing incidence diffraction (GID).[17]

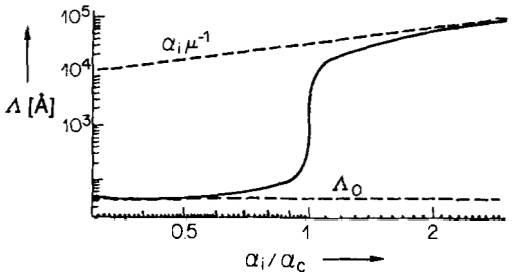

Fig. 2. X-ray beam penetration depth Λ in water at $\lambda = 1.38$ Å versus incidence angle α_i/α_c. The limiting value Λ_0 of the penetration depth for $\alpha_i/\alpha_c \ll 1$ is a characteristic materials constant, ($\Lambda_0 = (\pi r_0 \rho)^{-1/2}/4$), independent of the X-ray wavelength λ. For $\alpha_i/\alpha_c \gg 1$ the penetration depth is $\alpha_i\mu^{-1}$; the linear absorption coefficient μ *does* depend on λ.

In 3D crystals, diffraction from a set of crystal planes with an interplanar spacing d occurs only when the Bragg law is obeyed; namely when, firstly, the scattering vector length $|\boldsymbol{q}|$ (given by $|\boldsymbol{k}_f - \boldsymbol{k}_i| = 4\pi \sin\theta/\lambda$) is equal to $2\pi d^*$, where d^* is the reciprocal of the interplanar spacing d, and, secondly, the normal to the planes bisects the angle between the incident and outgoing beam. This condition may be mathematically expressed in terms of the reciprocal lattice vectors $\boldsymbol{d}^* = h\boldsymbol{a}^* + k\boldsymbol{b}^* + l\boldsymbol{c}^*$ where $\boldsymbol{a}^*$, $\boldsymbol{b}^*$, $\boldsymbol{c}^*$ are the reciprocal vectors of the unit-cell vectors $\boldsymbol{a}$, $\boldsymbol{b}$, $\boldsymbol{c}$, and h, k, l are integers that represent the Miller indices of planes with a spacing d_{hkl}. Diffraction therefore only takes place in 3D crystals when the scattering vector $\boldsymbol{q}$ coincides with (h,k,l) points of the reciprocal 3D lattice (Fig. 3c).

For a 2D crystal there is no selection rule or restriction on the scattering vector component $\boldsymbol{q}_z$ along the film normal. Thus the Bragg scattering extends as continuous rods (BR) through the 2D reciprocal lattice points[18] (Fig. 3b). The finite thickness of the 2D crystal causes the BR to extend over finite $\boldsymbol{q}_z$ intervals. The intensity distribution along these intervals is determined by the vertical electron density distribution in the molecules and is expressed as the Fourier transform of the resulting electron density along the film normal.

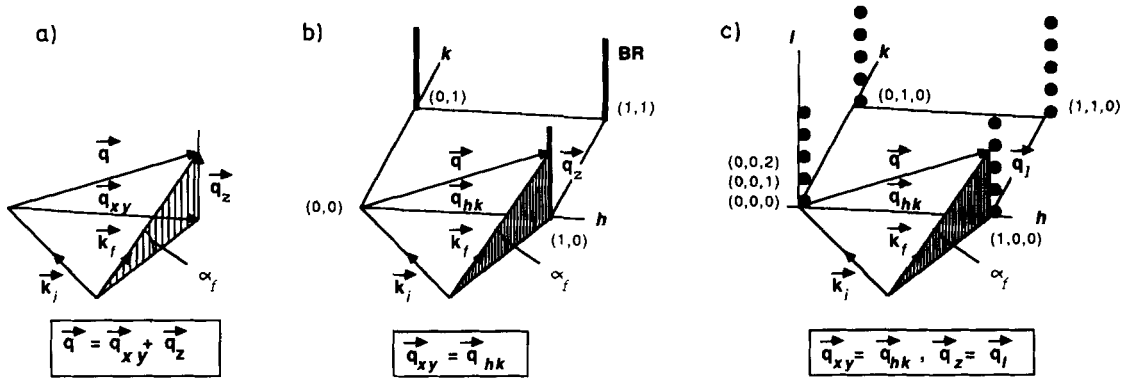

Fig. 3. a) General scattering geometry k_i and k_f are the wavevectors of the incident and diffracted beams respectively. The scattering vector $q = k_f - k_i$ has components q_{xy} parallel to the monolayer plane and q_z perpendicular to it. b) The scattering from a 2D crystalline material in reciprocal space extends in rods (Bragg rods) in the q_z direction, perpendicular to the plane of the monolayer and of its reciprocal 2D net. The scattering vector q must end on an (h,k) Bragg rod for Bragg diffraction. c) The scattering from a 3D crystal in a given orientation lies in reciprocal or q space at the reciprocal lattice points (h,k,l). Diffraction takes place when q coincides with a specific reciprocal lattice point [(1,0,3) in this particular case].

This intensity modulation can now be analyzed to obtain information, for example, on the direction and magnitude of the molecular tilt in the crystalline part of Langmuir monolayers.[19, 20] In addition, detailed information on the electron density distribution in the vertical direction, laterally averaged over both the ordered and disordered parts of the monolayer can be obtained from the deviation of the measured X-ray reflectivity[19, 21] (XR) from the Fresnel law.[16] By combining the methods of GID and XR, the structure of Langmuir films can be accurately characterized. Finally, grazing incidence X-ray excited fluorescence[22] and X-ray standing wave[23, 24] measurements yield information on the location and concentration of ions bound to the monolayer at the liquid interface. We now discuss these methods in some detail.

2.1. Specular Reflectivity (XR)

Specular reflection means that the reflected ray measured is in the plane spanned by k_i and the vector normal to the surface and that $\alpha_i = \alpha_r$ (see Fig. 1). The specular reflectivity of an ideal surface is given by the well-known Fresnel law of optics.[16] In the limit of small angle of incidence,[19, 21] applicable here, it reduces to Equation (3), where $q_z = (4\pi/\lambda)\sin\alpha_i$ is the z component of the momentum transfer and $q_c = (4\pi/\lambda)\sin\alpha_c$ is the critical value of q_z for total external reflection. The complex term arises from absorption effects (see Section 2). Neglecting absorption ($q_z < q_c$) Equation (3) yields $R_F = 1$, that is, total reflection. As q_z is increased beyond q_c, however, R_F decreases and, for $q_z \geq 4q_c$, approaches $R_F(q_z) \approx (q_c/2q_z)^4$. As the range of interest may extend to $q_z/q_c \approx 30$ or more,[19, 21] reflectivities down to 10^{-8} have to be measured. Hence the importance of high-intensity synchrotron sources or high-power rotating anode X-ray generators for XR measurements. Equation (3) is valid only for an ideally flat surface across which the electron density $\rho(z)$ varies steplike between two constant values. If $\rho(z)$ is not a step function, but varies continuously in the surface region, the reflectivity is modified,[19, 21] yielding Equation (4), where ϕ is defined as in Equation (5) and ρ_∞ is the constant electron density in the subphase bulk. Thus, by measuring $R(q_z)$ it is possible in principle to determine $\rho(z)$, the variation of the electron density normal to the surface, and, in particular, that of a monolayer floating on it. The function ϕ is complex, and only its modulus can be derived from the measured reflectivity but not its phase. Thus one is faced with the usual phase problem of X-ray crystallography and therefore to date virtually all specular reflectivity data has been analyzed by fitting a parametrized model density $\rho(z)$ to the measured data applying Equations (3), (4) and (5).

$$R_F(q_z) = \left[\frac{q_z - [q_z^2 - q_c^2 + i(4\pi\mu/\lambda)]^{1/2}}{q_z + [q_z^2 - q_c^2 + i(4\pi\mu/\lambda)]^{1/2}}\right]^2 \quad (3)$$

$$R(q_z) = R_F(q_z)|\phi(q_z)|^2 \quad (4)$$

$$\phi(q_z) = \frac{1}{\rho_\infty}\int \frac{d\rho(z)}{dz} e^{iq_z z} dz \quad (5)$$

One strategy has been to generate $\rho(z)$ as the sum of densities $\rho_i(z)$ from individual atoms at height $z = z_i$ and refine this *atomic model* of the monolayer molecules under suitable constraints.[25, 26] A typical constraint would be that, say, the hydrophobic moiety must tilt as a rigid body, that is, without distorting the a priori assumed internal bond lengths and angles. Adjustable parameters, then, would be the tilt angle of each molecular segment, the height of the molecule above the interface, and the area per molecule.

A computationally slightly simpler strategy presents the monolayer as a stack of slabs,[27] each with a constant density ρ_i and thickness l_i. Two such slabs would be needed for representing a simple fatty alcohol or acid monolayer.[28] When refining such a *slab model*, possible fit parameters would be the densities ρ_i and thicknesses l_i of the slabs.

For either representation of the monolayer, the constant density of the semi-infinite subphase has to be added below the interface. Finally, either model density must be smeared out in the z direction to account for the vertical roughness or diffuseness of the interface. The root-mean-square roughness, σ, is of order of 3 Å and stems mainly from thermally excited capillary waves on the water surface.[19, 21b, 21c] It leads to a Debye–Waller factor $\exp(-q_z^2\sigma^2)$ in $|\phi(q_z)|^2$ (Eq. 5)).

The rather large value of $\sigma \approx 3$ Å (equivalent in normal crystallographic parlance to $B = 8\pi^2\sigma^2 \approx 225$ Å^2) makes it unnecessary to use accurate charge densities for the atoms in the atomic model of $\rho(z)$, so long as each atom contributes its proper charge Z_i, the description will be adequate. Replacing groups of atoms by pseudoatoms is also feasible. Furthermore, since the value of σ is large, the monolayer may be adequately represented by the slab model. This is illustrated in Figure 4, which shows that the density $\rho(z)$ of a fatty acid monolayer may be represented by either model.

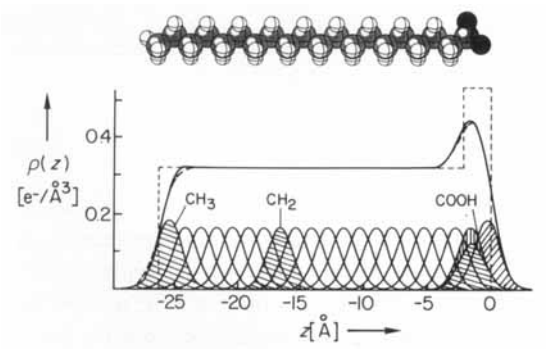

Fig. 4. Top: Space-filling model of a $C_{19}H_{39}CO_2H$ molecule. Bottom: Model electron densities $\rho(z)$. The dashed lines refer to a slab model and a smoothed slab model. The full lines refer to an atomic model using CH_3 and CH_2 as pseudoatoms. The contribution of each pseudoatom (or atom at the CO_2H head group) to the electron density is indicated by Gaussian curves. The two models agree nearly exactly even though drawn for display purposes with an unrealistically small smearing parameter σ of 1 Å.

2.2. Grazing Incidence Diffraction (GID) and Bragg Rods

In the GID geometry (Fig. 5) the angle of incidence α_i of the X-ray beam is kept below the critical angle α_c, limiting the penetration depth of the beam to that of the evanescent wave. Scattering due to the subphase is efficiently eliminated, which allows an accurate measurement of the weak diffraction signal originating from the crystalline monolayer. For all the diffraction patterns measured so far, the monolayers were found to be composed of 2D crystallites randomly oriented on the water surface, that is a 2D "powder". Hence

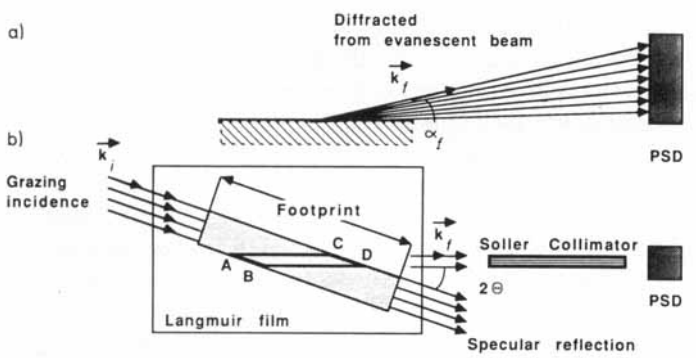

Fig. 5. a) Side and b) top view of the grazing incidence X-ray diffraction geometry. The footprint of the grazing incident beam is indicated by the shaded area. The position sensitive detector (PSD) has its axis along the vertical. Only the cross-beam area ABCD contributes to the measured scattering. The Soller collimator consists of thin vertical absorbing foils stacked together to define the horizontal resolution of the detector.

only a 2θ or q_{xy} scan in the monolayer plane is required to measure the diffraction pattern. The analysis is similar to that of a conventional 3D powder pattern; the reflections can be indexed by two Miller indices, h and k. Their angular positions $2\theta_{hk}$ corresponding to $q_{hk} = (4\pi/\lambda)\sin\theta_{hk}$ yield the repeat distances $d_{hk} = 2\pi/q_{hk}$ of the 2D lattice structure. Their resolution-corrected 2θ-line width (FWHM) Δ yields the 2D crystalline coherence length L through the well-known Scherrer formula [Equation (6)].[29]

$$L = \frac{0.9\,\lambda}{\cos\theta_{hk}\,\Delta} \tag{6}$$

Finally, the square of the molecular structure factor $|F_{hk}|^2$ integrated along the Bragg rod over the window of q_z seen by the detector determines the integrated intensity in the peak.[15] The structure factor F_{hk} is given by Equation (7),[18-20, 30a] where f_j is the scattering factor of the atom j, $\boldsymbol{r}_{x_jy_j}$ is the vector specifying the (x,y) position of the atom j in the unit cell and z_j is the atomic coordinate along the vertical direction.

$$F_{hk}(q_z) = \sum_j f_j e^{i(\boldsymbol{q}_{hk}\boldsymbol{r}_{x_jy_j} + q_z z_j)} \tag{7}$$

More information can be obtained by resolving the variation with q_z along the Bragg rod of the intensity $I_{hk}(q_z)$, given by Equation (8).[18-20, 30a]

$$I_{hk}(q_z) = |V(q_z)F_{hk}(q_z)|^2 e^{-q_z^2\sigma^2} \tag{8}$$

The observed BR intensity I is actually a sum over those (h,k) reflections whose Bragg rods coincide at a particular horizontal 2θ-angle or q_{xy} position.[18-20, 30a] In Equation (8), the most important variation is due to the molecular structure factor $|F_{hk}(q_z)|$. For the simple linear surfactant molecules considered here, the square of the structure factor $|F(\boldsymbol{q})|^2$ is a bell-shaped function which reaches its maximum when the scattering vector $\boldsymbol{q} = (\boldsymbol{q}_{hk}, \boldsymbol{q}_z)$ is orthogonal to the molecular axis. Thus, when the molecules are vertical or tilted in a plane perpendicular to $\boldsymbol{q}_{hk}$, the maximum intensity along the Bragg rod will occur at the horizon, for $q_z = 0$ Å^{-1}. For molecules tilted otherwise, we expect the Bragg rod maximum at a finite q_z, dependent upon both the magnitude and direction of the tilt relative to the in-plane scattering vector $\boldsymbol{q}_{hk}$. The width of the bell-shaped Bragg rod profile measured in a direction parallel to the molecular axis is inversely proportional to the length of the molecule.[19, 20]

The simple description of $F(\boldsymbol{q})$ alluded to above may be improved on by calculating $F(\boldsymbol{q})$ according to an atomic model of the molecule[20, 30a] [Eq. (7) and (8)]. For linear molecules, qualitatively similar results are obtained with both models.[20] The exponential factor [the vertical Debye–Waller factor, Eq. (8)] accounts for the internal thermal motion of the atoms in the molecule, as well as for ripples on the water surface, which lead to roughness of the interface.[19, 21b, 21c] The factor $V(q_z)$ describes the interference of rays diffracted upwards with rays diffracted down and subsequently reflected back up by the interface.[18a] $V(q_z)$ differs from 1 only in the vicinity of $q_z = 1/2\,q_c$, where it contributes a sharp peak to I (cf. Fig. 8 and the related discussion).

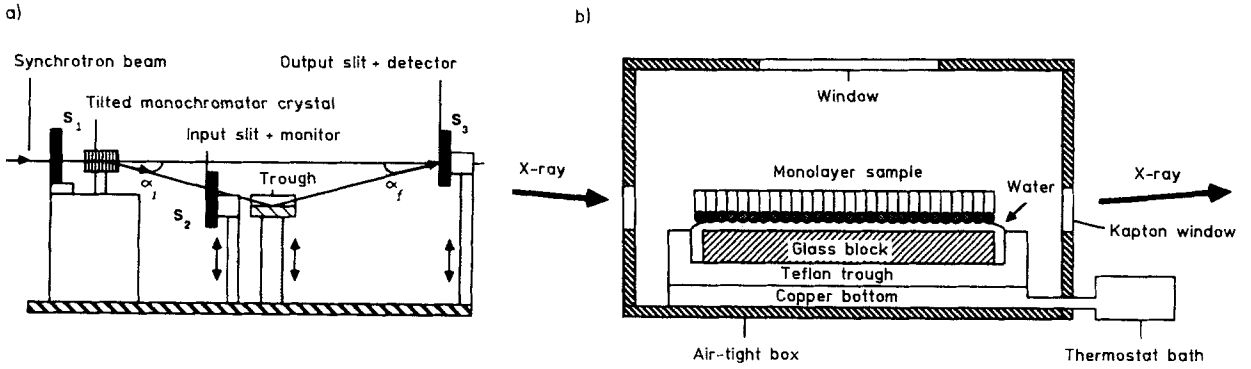

Fig. 6. Example of an experimental setup of a diffractometer for studying liquid surfaces (beamline D4, X-ray synchrotron source at Hasylab, Hamburg). a) Side view of the vertical scattering plane. Beam directions are defined by slits. The monochromatic beam is bent down towards the sample by tilting the monochromator crystal. The incident beam intensity is monitored beyond slit S_2. b) Enlarged view of the trough showing the monolayer sample spread on a thin film of water. The glass block guarantees a thin liquid film (about 0.3 mm thick) and thus effectively reduces surface capillary waves.

While both BR and XR data provide information on the vertical variation of the electron density, there are important differences between the two methods. The BR recorded at a given GID peak position originates solely from crystalline material. This is in contrast with XR, where the reflected signal is an average over *all* of the illuminated area regardless of coverage and in-plane structure. Furthermore, as the molecules in the contributing crystallites have a well-defined orientation relative to $\boldsymbol{q}_{hk}$, the BR profile depends very sensitively on the azimuthal direction of the molecular tilt. XR, on the other hand, averages over all azimuthal angles and hence provides no information on the molecular azimuthal orientation.

We now describe briefly a possible experimental setup (Fig. 6) for the diffraction geometry[31–33] shown in Figure 5. A suitable aperture S_1 is placed in the horizontal synchrotron radiation beam incident from the left (Fig. 6a). A monochromatic beam is selected from the "white" spectrum by Bragg reflection from a monochromator crystal, typically a perfect Ge crystal in the (111) orientation. By tilting the normal to the reflecting planes out of horizontal plane, the monochromatic beam can be bent down to yield a glancing angle with the horizontal liquid surface. The sample is mounted on an elevator so that the liquid surface always intersects the monochromatic beam. A narrow slit S_2 in front of the sample defines a suitable footprint of the beam on the liquid surface. The slit S_3 excludes diffuse scattered background around the reflected beam. This slit together with a scintillation detector is mounted on an elevator situated on a diffractometer arm which is pivoted around a vertical axis through the sample center. For in-plane diffraction measurements the slit S_3 is replaced by a Soller collimator giving 1 or 2 mrad collimation and the scintillation counter by a position-sensitive detector allowing Bragg rod measurements to be made (Fig. 5).

2.3. X-ray Fluorescence Methods

Atoms illuminated by X-rays of energy higher than that of their absorption edges will emit characteristic secondary radiation, the intensity of which is proportional to the number of excited atoms. Thus, by employing monochromatic X-rays of energy higher than, for example, the energy of the K absorption edge of a given ion dissolved in the subphase, it is possible to study the depth dependence of the concentration of that ion in the subphase. From Figure 2, we see that by varying α_i in the vicinity of α_c we can fine-tune the penetration depth of the primary radiation, and hence the depth to which we excite the ions dissolved in the subphase. Roughly speaking, the intensity variation of the secondary radiation will therefore follow the concentration variation with depth of the emitting ions.[34]

The method of near-total external fluorescence (NTEF) presented above provides information on the *vertical* concentration variation of the fluorescing probe ion. A variation on this method involves surface-EXAFS (Surface Extended X-ray Absorption Fine Structure, SEXAFS), where the fluorescence intensity variation is measured while varying the energy of the exciting radiation across the absorption edge of the probe atoms.[22] By keeping the angle of incidence α_i smaller than α_c, the penetration depth is kept to a few tens of Ångstroms. The short-range atom–atom correlation function in the surface layer (which gives a measure of interatomic distances) can be extracted by conventional EXAFS data analysis methods. By observing changes in this function induced by surface pressure variation in a deposited monolayer on the surface of the subphase, the interatomic distances in a layer of ions adsorbed from the subphase at its interface with the monolayer can be determined.[22] Thus a combination of NTEF and SEXAFS can be employed to provide information on both the vertical and horizontal structure of the probe ion near the surface. However, in contrast to GID, the in-plane information provided by SEXAFS is short range only and extends up to second nearest neighbors at most. On the other hand, GID is applicable only if reasonably long-range order exists (≥ 100 Å), while SEXAFS will provide average nearest-neighbor distances even for completely disordered systems.

2.4. X-ray Standing Waves

Standing waves are created when two coherent plane traveling waves are superimposed in the same region of space.[23] This is schematically depicted in Figure 7a, which shows the

resulting standing wave created by interference between an incident plane wave of vector $\boldsymbol{k}_i$ and its reflection from a mirror surface with a wavevector $\boldsymbol{k}_r$.

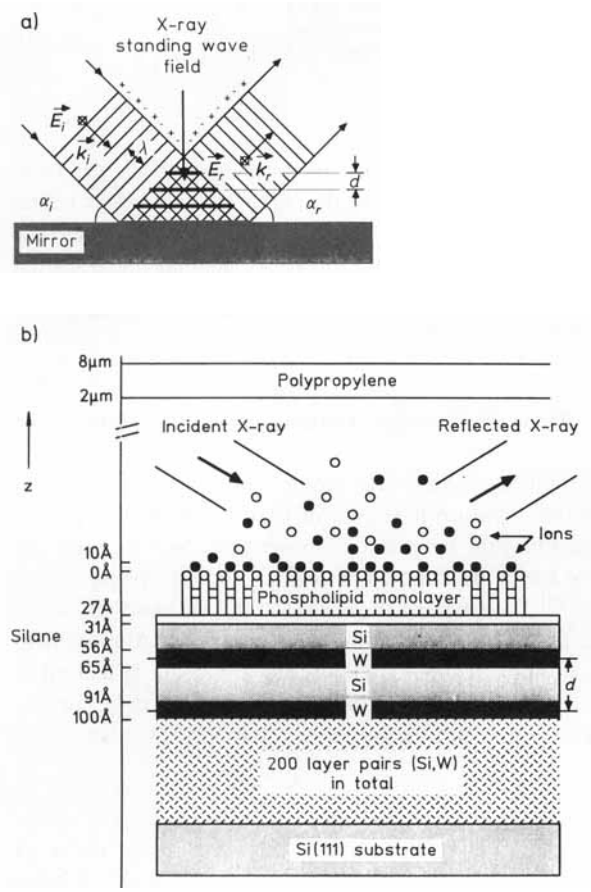

Fig. 7. a) Illustration of the X-ray standing wave field formed by the interference between the incident (E_i) and specular-reflected (E_r) plane waves above a mirror surface. By locating the intersections of the crests (labeled + lines) and troughs (labeled − lines) of the two plane waves, one can easily show that the antinodes of the standing wave are parallel to the mirror surface. Since total external reflection of X-rays (wavelength in Å range) occurs at incident angles α_i smaller than 0.5°, the spacing d typically varies between 100 Å and 1000 Å. b) Scheme showing a phospholipid monolayer deposited on a silanated Si/W layered synthetic microstructure (LSM). In the experiment depicted here [24b], the head group of the phospholipid containing an anionic phosphate group is exposed to solution and attracts zinc ions from a 0.1 mM $ZnCl_2$ aqueous solution. The polypropylene film traps a 2 μm thick water layer.

Conventionally, dynamical Bragg diffraction from perfect single crystals is used to generate an X-ray standing wave, whose period d is exactly commensurate with the diffracting planes of the crystal. For films adsorbed onto the crystal surface, with a thickness of say 20 to 100 Å, one requires long-period X-ray standing waves[24] which may be generated by Bragg diffraction from layered synthetic microstructures (LSM, Fig. 7b). For Bragg diffraction purposes a LSM is fabricated as a periodic layered structure consisting of 10 to 200 layer pairs of alternating high and low electron density materials (such as tungsten and silicon) to yield a diffraction plane spacing varying from 20 to 200 Å (Fig. 7b). Long period X-ray standing waves are also generated by total external reflection when the incident angle is less than the critical angle α_c (Fig. 7a). The period of the standing waves is $d = \lambda/2\sin\alpha_i$.

To measure the effect of standing waves, an energy-dispersive detector is positioned above the surface and picks up the X-ray fluorescence from atoms adsorbed at the crystal surface or close to it. The fluorescence radiation of these atoms will depend on their positions as the period and phase of the standing wave changes with the angle of incidence of the primary beam. Figure 7b depicts an interesting application of the technique to ion–surfactant interactions: the study of interfaces between adsorbed charged monolayers and the distribution of the counterions in solution.[24b]

3. General Packing Characteristics of Langmuir Monolayers on Water

Before the development of surface X-ray diffraction techniques, knowledge of molecular arrangement in the three-dimensional state was used to increase understanding of the structure and behavior of molecules in the monolayer state, as already mentioned in Section 2. Analogous packing is not always possible however, because of environmental differences between the two- and three-dimensional states. Phase diagrams constructed from surface pressure–area (π–A) measurements for such compounds revealed phase boundaries, depending upon pressure, temperature, and chain length, but could provide little information on the structure of these phases. Now, with recently acquired information from surface-sensitive X-ray techniques, the packing of such Langmuir films can be determined almost at atomic level. Although GID measurements have been carried out on several Langmuir monolayer systems, the monolayer structures corresponding to the complete phase diagrams have been elucidated by GID only for the acids $C_{20}H_{41}CO_2H$ and $C_{21}H_{43}CO_2H$, discussed in Section 3.2. In Section 3.1 we describe one or two examples from each chemical class studied to date: alcohols, amides, carboxylic acids, divalent salts of the latter, α-amino acids, and phospholipids (see Table 1 for their chemical formulas and abbreviations). The latter two classes of compounds possess an asymmetric carbon atom whose chirality is specified by the symbol (*R*) or (*S*).

Table 1. Abbreviations for monolayer compounds discussed here and their chemical formulae

Abbreviation	Full Name	Chemical Formula
C_nOH	aliphatic primary alcohols	$C_nH_{2n+1}OH$
C_nCO_2H	aliphatic primary acids	$C_nH_{2n+1}COOH$
C_nCONH_2	aliphatic primary amides	$C_nH_{2n+1}CONH_2$
$C_{19}CONHC_2H_4CO_2H$	*N*-arachidoyl-β-alanine	$C_{19}H_{39}CONHC_2H_4CO_2H$
DMPE	dimyristoyl-phosphatidylethanolamine	$C_{13}H_{27}COOCH_2CH(OOCC_{13}H_{27})$-$CH_2PO_4^-$, $C_2H_4NH_3^+$
PL	palmitoyl-lysine	$C_{15}H_{31}CONHC_4H_8CHNH_3^+CO_2^-$
PFA	"perfluoro"dodecyl-aspartate	$C_{10}F_{21}C_2H_4OCOCH_2CHNH_3^+CO_2^-$

It is useful at this stage to describe how unit cell dimensions and molecular orientation may be determined from GID data for simple cases. We consider the molecule as a freely rotating alkane chain; in other words, it has cylindrical symmetry. These molecules may pack in three different cell types: hexagonal ($a = b$, $\gamma = 120°$), distorted hexagonal ($a =$

b, $\gamma \neq 120°$) which may be more properly described as centered rectangular ($a' = |\boldsymbol{a} + \boldsymbol{b}|$, $b' = |\boldsymbol{a} - \boldsymbol{b}|$), and oblique ($a \neq b \neq |\boldsymbol{a} + \boldsymbol{b}|$) (Fig. 8). The molecules in a hexagonal cell are aligned vertically relative to the plane of the film, while in the distorted hexagonal cell they are tilted along a symmetry direction and in the oblique cell along an arbitrary direction. As mentioned earlier, all Langmuir monolayers studied

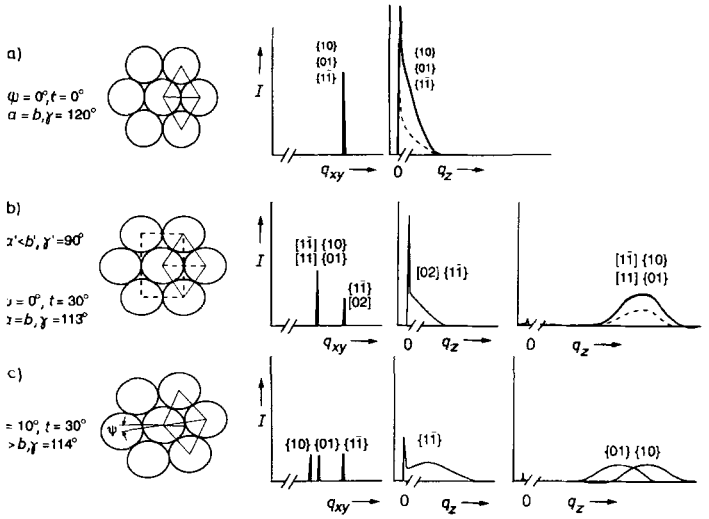

Fig. 8. Three possible structures and diffraction from a monolayer of close-packed, freely rotating alkyl chains. The left column shows schematic top views of the molecular packing in hexagonal, distorted hexagonal, and oblique unit cells. The second column shows the q_{xy}-pattern integrated over the vertical wavevector component q_z, and the last two columns show the Bragg rods integrated over the corresponding q_{xy}. When more than one reflection coincide, the dashed lines represent the intensity from individual reflections as indicated by the Miller indices. The solid line represents the intensity from a two-dimensional powder sample; that is, the sum of the intensities indicated by dashed lines. When the molecular axis is perpendicular to the water surface the lattice is hexagonal [a)], and the $\{1,0\}$, $\{0,1\}$ and $\{1,\bar{1}\}$ reflections are degenerate. The Bragg rod obtained from the single in-plane diffraction peak has its maximum at $q_z = 0\,\text{Å}^{-1}$. When the molecular axis is tilted towards nearest neighbors [b)], the hexagonal structure is distorted to a centered rectangular structure (rectangular notation at the top, distorted hexagonal notation at the bottom). The degeneracy of the three reflections is partially lifted resulting in two peaks. The Bragg rod of the two degenerate reflections $\{1,0\}$ and $\{0,1\}$ ([1,1], $[1,\bar{1}]$ in the rectangular notation) is centered at $q_z \geq 0\,\text{Å}^{-1}$. The Bragg rod of the $\{1,\bar{1}\}$ reflection ([0,2] in the rectangular notation) is still centered around $q_z = 0\,\text{Å}^{-1}$. Finally, when the molecular axis is tilted in a non-symmetry direction, the intersection between the close-packed circular chains and the water surface forms an oblique 2D lattice [c)]. The degeneracy is completely lifted and the peak positions of the three Bragg rods determine the tilt angle as well as the azimuthal angle Ψ unambiguously.

to date by GID consist of "powders" of randomly ordered 2D crystallites on the water surface so that the GID measurements are not made on single crystals. Thus, the diffraction spectra consist of coinciding Bragg rods of reflections (h,k,q_z) and $(\bar{h},\bar{k},q_z)$, the notation $\{h,k,q_z\}$ designating both reflections. In general, the intensity distribution along their two coinciding Bragg rods will be different unless the monolayer structure has twofold symmetry along the vertical axis.

The hexagonal cell has three equivalent lattice spacings d_{hk}: d_{10}, d_{01}, and $d_{1\bar{1}}$. The GID spectrum from these three reflections will appear as a single signal with all corresponding Bragg rods peaking at $q_z = 0\,\text{Å}^{-1}$ (Fig. 8a). The corresponding GID spectrum for the distorted hexagonal cell will comprise two peaks; one a superimposed doublet arising from the coinciding $\{1,0\}$ and $\{0,1\}$ reflections, and the other the remaining $\{1,\bar{1}\}$ peak (Fig. 8b). The separation between

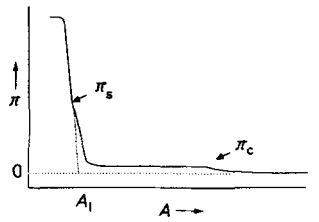

Fig. 9. General shape of a surface-pressure versus area isotherm (π–A isotherm) of a Langmuir monolayer. A_l is defined as the limiting area (i.e., the close-packed area for the molecules at zero pressure). π_s and π_c define transition pressures between phases.

the two peaks depends upon the deviation of the angle γ from 120°. In the oblique cell the degree to which the three reflections $\{1,0\}$, $\{0,1\}$, and $\{1,\bar{1}\}$ are resolved (Fig. 8c), depends upon the deviation from centered rectangular (i.e. distorted hexagonal) cell symmetry.

3.1. Phase Changes Induced by Surface Pressure

A typical pressure–area isotherm of Langmuir films at room temperature is shown in Figure 9. It has long been realised that the kinks in the isotherm (the surface pressures at the kinks are denoted π_c and π_s) indicate phase transitions.[10] The shape of the isotherm and the positions of the kinks are characteristics of a given monolayer. At room temperature the alcohol $C_{21}OH$ and acid $C_{20}CO_2H$ as well as the α-amino acid PFA exhibit isotherms with only one distinct kink at π_s (in the range 15–30 mN m^{-1}), whereas the

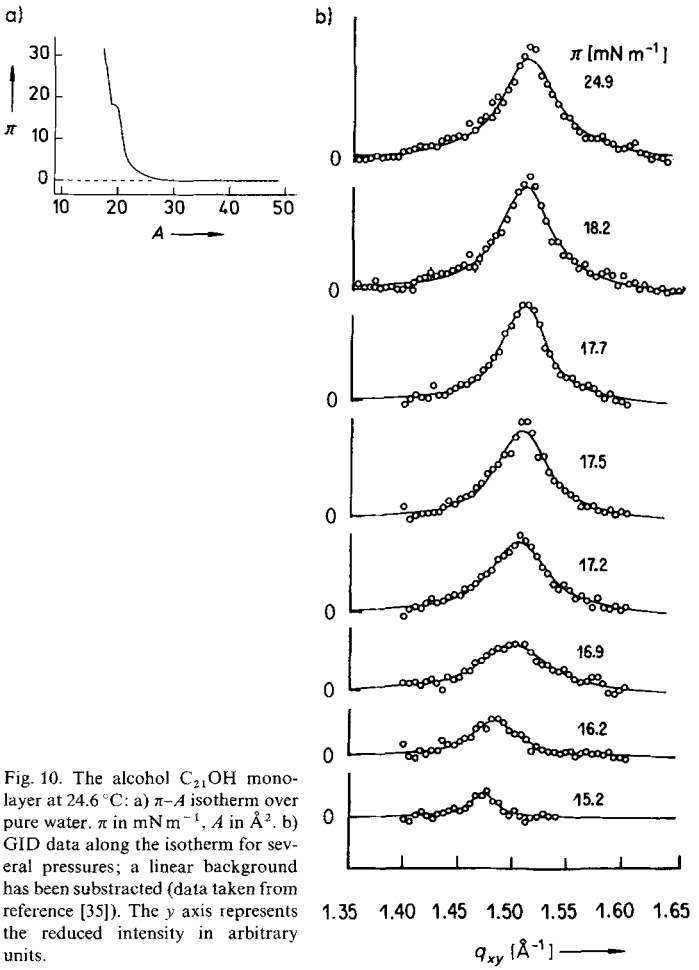

Fig. 10. The alcohol $C_{21}OH$ monolayer at 24.6 °C: a) π–A isotherm over pure water. π in mN m^{-1}, A in Å^2. b) GID data along the isotherm for several pressures; a linear background has been substracted (data taken from reference [35]). The y axis represents the reduced intensity in arbitrary units.

phospholipid compound DMPE has an isotherm with two kinks (π_c in the range 5–10 mN m^{-1} and π_s in the range 20–30 mN m^{-1}). The α-amino acid PL shows no observable kink. It has generally been assumed that a decrease in molecular area induces transitions from gaseous through "liquid-expanded" and "liquid-condensed" to the solid crystalline phases.[10] But the GID data on some systems reveal high crystallinity in the uncompressed state and a tendency towards a reduction of crystallinity with increased pressure. Thus, GID and XR results provide a more accurate description of the phases.

3.1.1. *Fatty Acids and Alcohols*

GID data for henicosanol[35] $C_{21}OH$ shows a single peak in the surface pressure range 15–30 mN m^{-1} and temperature range 15–30 °C (Fig. 10b). The changes in the peak with pressure observed at 24.6 °C (Fig. 10b) are typical of the isotherms measured (Fig. 10a). The gradual loss of intensity below π_s was interpreted[35] as being due to the appearance of *gauche* defects in the hydrocarbon chain. The kink then represents the lowest pressure at which the last of the gauche configurations are squeezed out. At higher pressures all the molecules stand straight with their hydrophobic tails in all-*trans* conformation.

Combined GID, Bragg rod, and XR room temperature measurements on arachidic acid[19,28] $C_{19}CO_2H$ along the isotherm (Fig. 11) have been interpreted differently; the drop in GID intensity as a function of decreasing surface pressure was accounted for by a continuous change in tilt of rigid parallel molecules.

The low pressure structure was assigned to a distorted hexagonal cell, where molecules tilt toward nearest neighbors. Such a cell yields two diffraction peaks, one corresponding to the $\{1,\bar{1}\}$ reflection and the other to $\{1,0\}$ and $\{0,1\}$. The results reported[35] for $C_{21}OH$ could possibly be interpreted in a similar manner. A definitive answer would require BR and XR measurements of that system.

The GID and XR results for $C_{19}CO_2H$ on pure water allows us to deduce some information on the packing of the carboxyl groups in the compressed ordered state at room

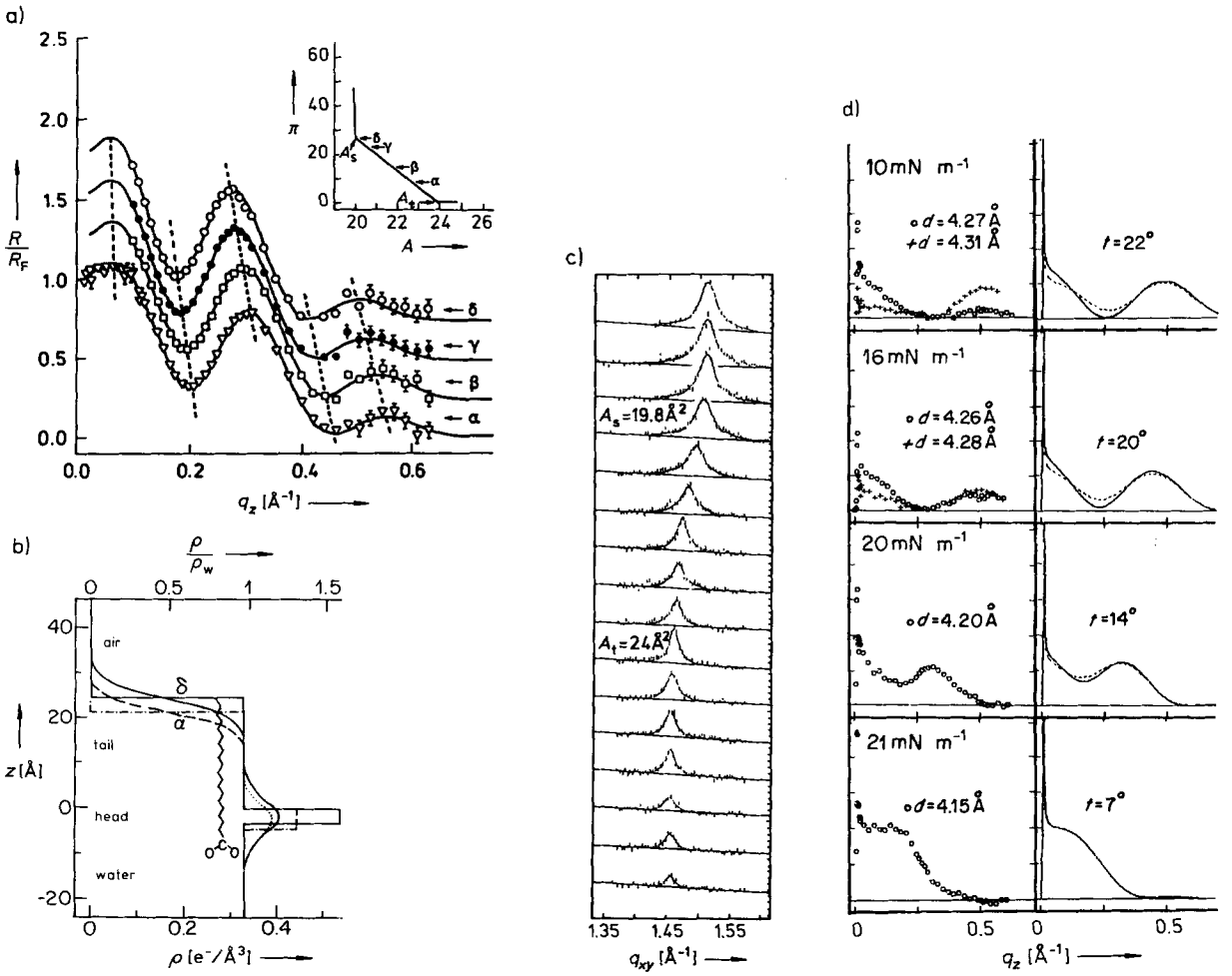

Fig. 11. Arachidic acid $C_{19}CO_2H$ monolayer at room temperature and over pure water: a) Normalized X-ray reflectivity (XR) data for increasing surface pressure (α–δ). The insert shows the π–A isotherm (π in mN m^{-1} and A in Å^2) of the monolayer and indicates the points where the XR measurements were performed. b) Fitted model of the vertical electron density $\rho(z)$. On compression, the monolayer thickness increases while the density remains constant in the tail region as shown by the change from the dashed lines to the full lines. $\rho_w = \rho_{water}$. c) GID data for decreasing mean molecular area; A_s and A_t correspond to the areas marked on the π–A diagram. d) Left: 2D powder Bragg rods observed at surface pressure of 10, 16, 20, and 21 mN m^{-1}. At 20 and 21 mN m^{-1}, the optimal q_{xy} settings for the merging peaks at $q_z = 0$ Å^{-1} and $q_z > 0$ Å^{-1} coincide, but for lower surface pressures they split as indicated by open circles (optimum q_{xy} for $q_z = 0$ Å^{-1}) and crosses (optimum q_{xy} for $q_z = 0.5$ Å^{-1}). Right: Calculated Bragg rod profiles from a slab model in which the molecules tilt towards next nearest neighbors by an angle t. The model parameters were determined essentially from the reflectivity data. The dashed line represents a perturbation of this model: the molecules were tilted in a direction 8° from the symmetry direction.

temperature. The hexagonal cell may at first sight imply complete rotational disorder about the chain axis. Indeed such structural disorder may be assumed for the alcohol $C_{21}OH$. However aliphatic carboxylic acids can hardly support such disorder for it could lead to a short contact $d_{O\cdots O}$ of about 1.5 Å between two adjacent oxygen atoms with their lone-pair electrons directed at each other (Fig. 12). Numerous studies[36] have demonstrated that two such adjacent oxygen atoms have a preferred separation of 3.5 Å. Whether hindered rotation of the acid molecules precludes a hexagonal symmetry (but not a hexagonal cell) is therefore a moot point.

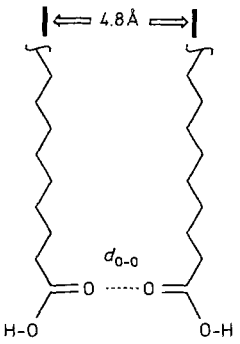

Fig. 12. Close contact ($d_{O\cdots O}$ spacing) between adjacent oxygen atoms of two fatty acid molecules separated by 4.8 Å and related by twofold symmetry.

3.1.2. *Phospholipids*

The extensive surface X-ray studies on phospholipid monolayers have been reviewed in detail in terms of structural changes along the π–A isotherm.[32, 37] We therefore confine this discussion to a brief review of some aspects of the condensed monolayer of α-dimyristoyl phosphatidylethanolamine (DMPE, see Table 1) from the view point of molecular packing (the isotherm is shown in Fig. 13a).

GID measurements[32] yielded a single peak in the pressure range between 10 and 38 mN m^{-1}. The variation with surface pressure of the diffraction peak characteristics is depicted in Figure 13b. The diffraction data for $\pi_c < \pi < \pi_s$ is consistent with coexistence between a nondiffracting liquid phase and a gel phase where the coherence length L increases with pressure. In the condensed phase (above π_s) the coherence length is no more than about 50 lattice distances, so the monolayer forms some crystalline solid phase, but with many defects. For the condensed phase region, the results of the X-ray reflectivity data (Fig. 13c) may indicate an ordering of the head groups.

Although little is known on the packing arrangement of hydrophobic chains and the hydrophilic head group PO_4^--CH_2-CH_2-NH_3^+ moieties, information thereon may be gleaned from the three-dimensional crystal structure of the racemic dilauryl derivative (*rac*-DLPE) whose packing arrangement[38] is shown in Figure 14. The most intense reflection from the layer structure of *rac*-DLPE has a spacing of 4.2 Å, which is the same value as that of the single GID peak observed from the chiral resolved compressed monolayer of DMPE (Fig. 13b, bottom), indicating a similarity in packing of their hydrophobic chains. In the 3D crystal the molecules

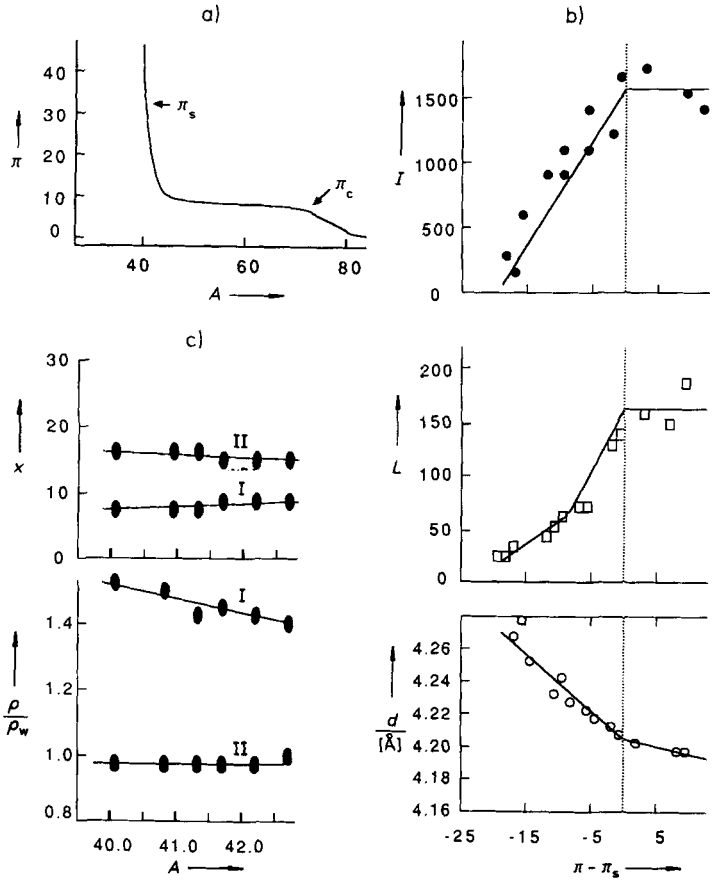

Fig. 13. Phospholipid DMPE monolayer over pure water at room temperature: a) π-A isotherm of DMPE; π in mN m^{-1}, A in Å^2. b) Three parameters extracted from the GID data as a function of surface pressure; the intensity of the integrated GID peak (I in arbitrary units), the coherence length L, and the lattice spacing d. c) Model parameters for the head (I) and tail (II) slabs [thickness x [Å] and electron densities $\rho(z)$ relative to that of water (ρ_w)] used in XR data fitting.

form a bilayer; within each layer the head groups are interlinked by NH···O hydrogen bonds by translation and glide symmetry. This head group packing is also observed in the crystal structure of (2-aminoethyl)phosphate HO–PO_3^-–

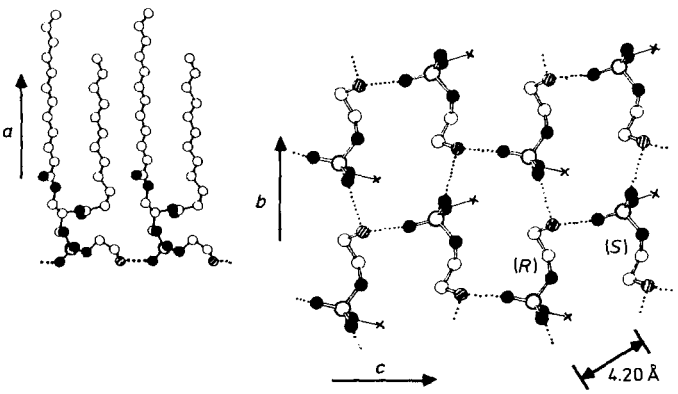

Fig. 14. The layer structure of *rac*-DLPE in its 3D crystal. The hydrogen atoms are omitted. Left: View down the c axis. Right: View down the a axis. For clarity each hydrocarbon chains are represented by a small cross. The molecules are interlinked by NH···O hydrogen bonds (dashed lines) by translation symmetry along the b axis (molecules of the same configuration) and by glide symmetry along the c axis (molecules of the opposite configuration). Note the characteristic 4.20 Å spacing imposed by the molecular packing. ● = O, ⊘ = N, o = C,P.

CH_2–CH_2–NH_3^+.[39] It is tempting to think that the head groups of chiral resolved monolayers of DMPE and DLPE would also pack in a pseudoglide arrangement. However, the monolayer study of DLPE and DMPE was performed on the resolved naturally occurring (*S*) enantiomer. Furthermore, the thickness of the layer of the head groups in the 3D crystal structure is 5.5 Å, but in the range of 7.15 to 9.5 Å in the monolayer structures according to the XR data.

3.1.3. α-Amino Acids

The α-amino acid surfactants were used for the oriented crystallization of the α-polymorph of glycine and of NaCl at the monolayer–solution interface (see Section 5). GID and XR measurements were performed on two of these monolayers in order to establish independently the similarity or complementarity of the head-group arrangement of the monolayer molecule and the layer arrangement of the crystal face attached to the monolayer.[25, 26, 30] Here we describe the packing characteristics of two α-amino acid surfactants, PL and PFA (see Table 1).

Palmitoyl-lysine (PL): The NH···O hydrogen bonding arrangement of the α-amino acid head groups NH_3^+-CH-CO_2^- and of the amide groups CO-NH in the chain essentially fixed the monolayer packing. The π–*A* isotherm of the monolayer of PL is shown in Figure 15a. A compressed (about 25 mN m^{-1}) monolayer of PL was found by GID to form crystalline domains with a coherence length of about 500 Å. The diffraction pattern[25] shows two Bragg peaks (Fig. 15c). The calculated GID positions and intensities for the model structure[25, 40] are also shown. Analysis of observed XR data (Fig. 15b) yields a tilt angle of the molecular chain axis of about 30° from the vertical. The deduced cell axes and packing arrangement of PL is shown in Figure 16. The α-amino acid head groups NH_3^+-CH-CO_2^- are arranged in a manner similar to that of crystalline α-glycine or other naturally occurring hydrophobic α-amino acids.[41–43] The linear NH···O hydrogen bonds between amide groups in the chain linking neighboring molecules along the (***a*** + ***b***) director (Fig. 16b) require a 30° tilt of the chain axes, as was independently deduced from the XR analysis.

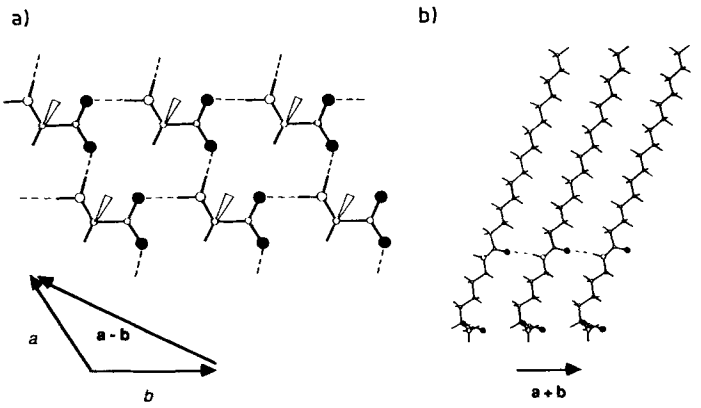

Fig. 16. Views of the model packing arrangement of (*R*)-PL monolayers over pure water; π = 25 mN m^{-1}. a) Perpendicular to the monolayer plane, the hydrophobic chain is represented by a wedge. The NH···O=C(acid) hydrogen bonds are symbolized by dashed lines. b) View along the ***a*** − ***b*** axis showing molecules in a row parallel to the ***a*** + ***b*** direction, interlinked by NH···O=C (amide) hydrogen bonds. ● = O.

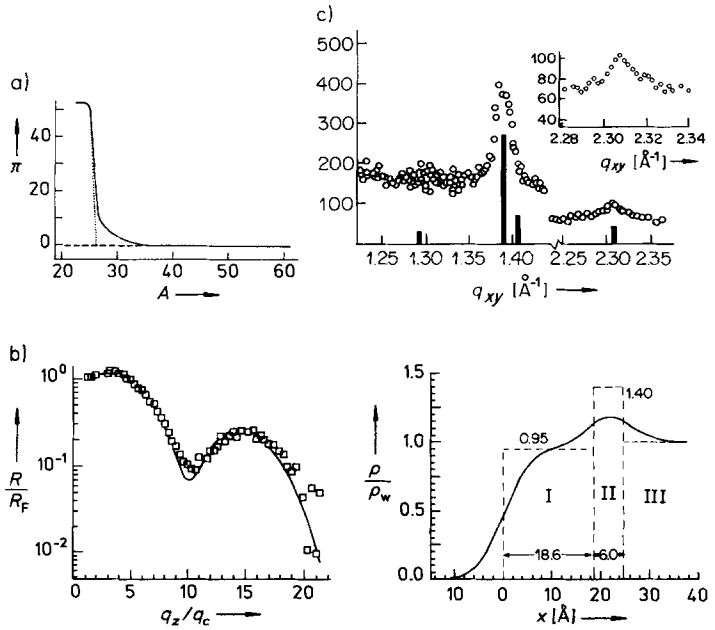

Fig. 15. (*R*)-PL monolayers over pure water at room temperature. a) π-*A* isotherms (π in mN m^{-1} and A in Å^2). b) Left: The measured, normalized *R* values and the theoretical model obtained by curve-fitting. Right: The refined model electron density $\rho(z)$ relative to that of water ρ_w. The PL molecules are modeled by two slabs, one corresponding to the head group (region II) and the other to the hydrocarbon tail (region I). Region III corresponds to the water subphase and z represents the height coordinate. The smoothed model shown as a solid line is obtained with a smoothing factor σ of 3 Å. c) GID of a compressed PL monolayer. The calculated relative intensities of the model (Fig. 16) drawn underneath the peaks are without adjustable parameters except for scale and Debye–Waller factors.

"Perfluoro"dodecylaspartate (PFA): The behavior of PFA upon compression is similar to that of arachidic acid in that the molecular tilt angle is continuously reduced with increasing surface pressure.[30a] However, the system revealed some original features. At low surface coverage (points α, β, γ on the isotherm in Fig. 17a), molecules of PFA self-assemble in large crystalline domains, in which they are arranged in an oblique cell and tilted by about 22° from the surface normal towards nearest neighbors (Fig. 18), as deduced from the three observed reflections in Figure 17d. Upon compression the three peaks first merge into a doublet (Fig. 17c) and then into a singlet (Fig. 17b), indicating that the symmetry of the cell, but not of the monolayer structure, goes from oblique (Fig. 17d), through distorted hexagonal (Fig. 17c), to hexagonal (Fig. 17b; see also Fig. 8 and the related discussion).

The molecular behavior of monolayers of PFA during a compression–decompression cycle can be explained with a knowledge of the head-group packing before compression.[30a] The hydrogen-bonding pattern of the α-amino acid head groups of uncompressed PFA was constructed from the known motifs of the 3D crystal structures of neopentylglycine,[5b] (*S*)-alanine,[44] and *rac*-alanine.[45] The major feature of this motif is the participation of intercalated, ordered water molecules interlinking adjacent hydrogen-bonded ribbons of PFA molecules (Fig. 18). The molecular area, which is dictated by the head group, is 30.9 Å^2 as compared with the cross-sectional area of the fluorocarbon chain

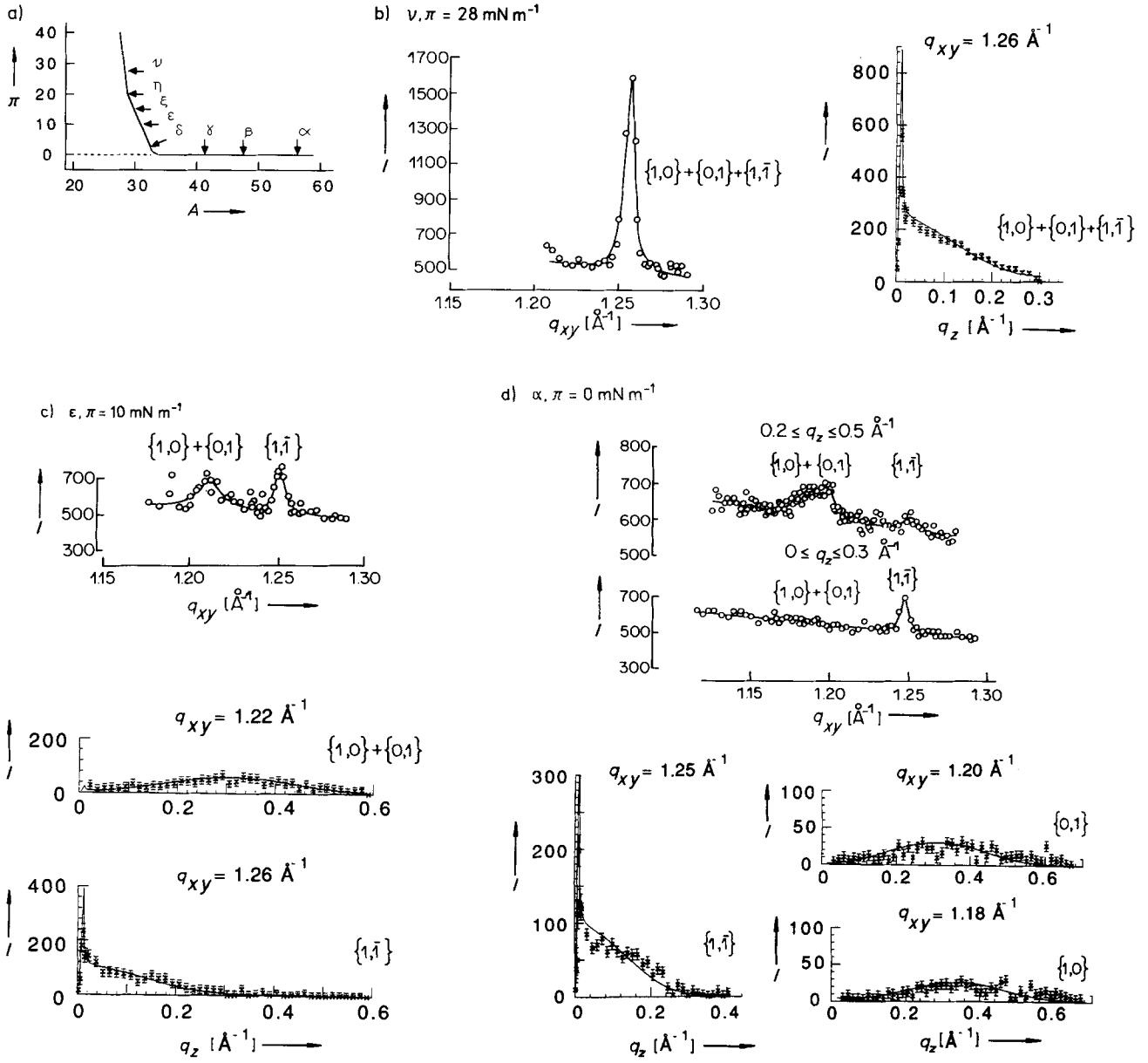

Fig. 17. PFA monolayers over pure water at room temperature. a) π-A isotherm (π in mN m^{-1} and A in Å^2). The points (α–ν) indicate where GID measurements were made. (b–d) A selection of GID measurements positions, ν, ε, and α) confirming the three observed 2D crystal symmetries (see also Fig. 8) when increasing the surface pressure. Left (b) or top (c,d): GID peaks. The Miller indices are indicated. Bottom: Bragg rod profiles measured on the GID peaks. Reflection positions and indices are given. Note that for position α in d) the GID peaks were measured for two different q_z intervals; furthermore, the Bragg rod intensity profiles have a different scale than in b) and c). In all cases, the solid line is the model fitted to the data. I = intensity in counts.

(28.5 Å^2). Upon increasing the pressure the molecular area is reduced and the water molecules are probably partially squeezed out of the hydrogen-bonded layer. At high pressure, hexagonal cell dimensions are imposed by the close contact between the fluorocarbon chains. Release of the surface pressure causes a dramatic decrease in coherence length L, an increased tilting of the molecules, and finally the disappearance of any observable diffraction, which is probably linked to the dynamics of the building process of a new bonding layer akin to the original one.

3.1.4. *Enantiomeric Mixtures of α-amino Acid Monolayers*

A little of the opposite enantiomer present in the chiral resolved monolayer of PL causes the GID peak to disappear (Fig. 19a). This indicates that the lattice of the monolayer becomes sufficiently distorted to reduce the crystalline coherence length drastically. The effect was explained by the inclusion of say an (*S*) molecule in a lattice of (*R*) molecules. Figure 19b shows that to reduce the resulting bad intermolecular contacts, the structure becomes distorted. Thus an appreciable fraction of the molecules in the monolayer are misaligned when even as little as 3% of the opposite enantiomer is added. The pure racemate also did not give a diffraction pattern at room temperature. Here we might have expected an arrangement in which the (*R*) and (*S*) molecules are interlinked in a layer by glide symmetry as observed in the crystal structure of hydrophobic *rac*-α-amino acids.[15, 45] We cannot rule out small ordered domains of this type in the solid solution of a pure PL racemate.

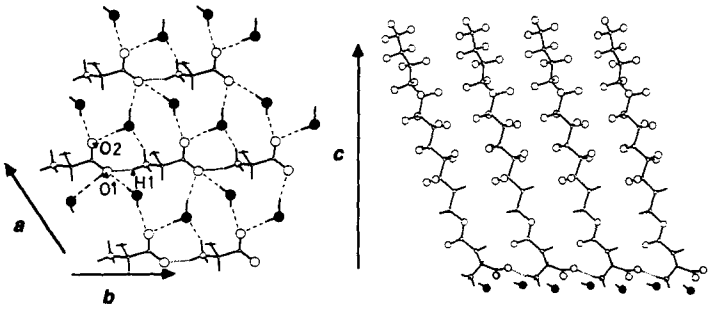

Fig. 18. Model of the arrangement of the self-assembled crystallites of a PFA monolayer over water at $\pi = 0\,mN\,m^{-1}$. Left: View perpendicular to the monolayer (i.e., along the c axis), showing hydrogen bonding of head groups and water molecules. O1 and O2 are oxygen atoms of the carboxylate groups; each forms hydrogen bonds with two water molecules. O1 forms a hydrogen bond with H1 of the NH_3^+ moiety of the neighboring molecule. The molecular chains are omitted for clarity. Right: View along the a axis showing the attached layer of water molecules and the projection of the chain tilt in the $(1,\bar{1})$ plane. • = oxygen atoms of the water molecules.

In contrast, the molecular area of compressed PFA monolayers (28.5 Å^2) imposed by the perfluorinated chain is larger than the molecular area observed in compressed monolayers of PL (24.3 Å^2) or in the crystal structure of glycine (25.5 Å^2). Therefore the more open head group arrangement of PFA is in keeping with the observation that racemic mixtures of compressed PFA display a very intense diffraction peak.[40b]

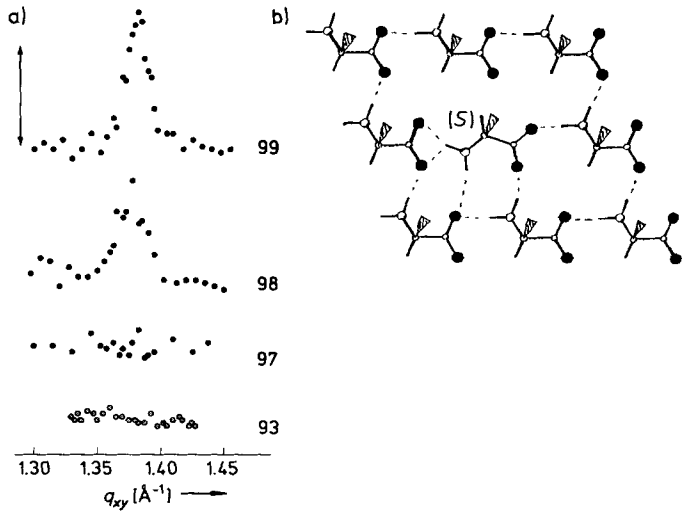

Fig. 19. a) GID data of mixed chiral monolayers of PL. The percentage of the (*S*)-enantiomer in the mixture is indicated on the right. The length of the double-sided arrow represents 200 counts. b) A PL molecule of (*S*) configuration surrounded by PL molecules of the opposite (*R*) configuration in a possible packing arrangement. All the chains are assumed to be related by translation and are indicated by wedges, so that the distortion of the hydrogen bonding (- - -) around the (*S*) isomer is visible. • = O.

Addition of the opposite enantiomer does not affect the crystal packing of PFA as it does for PL, since the distortion introduced in the hydrogen-bonding at the head group does not play a decisive role in the molecular packing of the compressed PFA monolayers.

3.2. Phase Changes Induced by Temperature

There is a wealth of macroscopic data available on temperature-induced phase transitions in Langmuir films, yet little reliable structural information on the molecular level. Only recently is such information becoming available from GID data. For example, the results on monolayers of fatty acids and fatty alcohols indicate a reduction in rotational disorder when the temperature decreases. Indeed, the diffraction pattern at high surface pressures (30 $mN\,m^{-1}$) for Langmuir films of the alcohol $C_{21}OH$ and the carboxylic acid $C_{20}CO_2H$ upon cooling from 30 °C to 0 °C shows additional peaks (Fig. 20a,b), indicative of a change from hexagonal to a centered rectangular cell.[46] The change was attributed to a pronounced reduction of librational motion of the molecule about its chain axis. Diffraction data on the acid monolayers $C_{21}CO_2H$[47] and $C_{29}CO_2H$,[48] and on the alcohols $C_{23}OH$, $C_{30}OH$, and $C_{31}OH$[48] at a temperature of 5 °C in the compressed state showed that the molecules of the film are vertically aligned.

The phase diagrams of the homologous series of long-chain fatty acids C_nCO_2H have been studied by means of pressure–area isotherms.[49] The phase diagrams of the series seem to be almost identical, provided that the temperature scale is shifted by 5–10 °C for each additional CH_2 moiety: extending the chain length has the effect of lowering the temperature. The available GID data,[19, 28, 47, 50, 51] taken as a whole, seem to confirm this conjecture. The phase diagram of docosanoic acid ($n = 21$) is reproduced in Figure 21. The acid $C_{21}CO_2H$ is convenient because nearly all the phases are observable at temperatures between 5 and 30 °C. Two independent synchrotron GID studies determined the structure of all the phases of docosanoic acid[47] and henicosanoic ($n = 20$) acid.[50] As the diffraction results were similar, we report here only those observed with docosanoic acid monolayers.

In each phase, the molecules are oriented with their long axes parallel and form a 2D crystal structure (Fig. 21), albeit with positional coherence lengths ranging from 50 Å at high temperature to more than 1000 Å at lower temperatures. The higher temperature structures may be similar to the mesophases found in liquid crystals. The L_2 phase has molecules tilted towards nearest-neighbors on a centered-rectangular net. On compression, at temperatures above ca. 25 °C one enters through a second-order phase transition into the hexagonal phase LS with vertical molecules. At these temperatures, indirect evidence suggests that the molecules are free rotators. At lower temperatures, compression leads from the L_2 phase through a first-order phase transition to the L_2' phase, again with tilted molecules on a centered-rectangular net, but with the molecules inclined towards next-nearest neighbors. Further compression leads to the phase S with vertical molecules on a centered-rectangular net. We note that lowering the temperature has the effect of reducing the symmetry of the high pressure phase from hexagonal (LS phase) to distorted hexagonal (S phase). One may speculate that the symmetry is reduced because the molecules have become hindered rotators. Below ca. 10 °C at high pressure, one observes the CS phase which has the same symmetry as the S phase. The CS phase, however, has long positional coherence lengths (> 1000 Å), a small area per molecule (18.6 Å^2), and a very low compressibility. It may be compared to 3D crystalline structures of alkanes well below their melting points, in which the molecular backbones are locked in a herringbone pattern.[52]

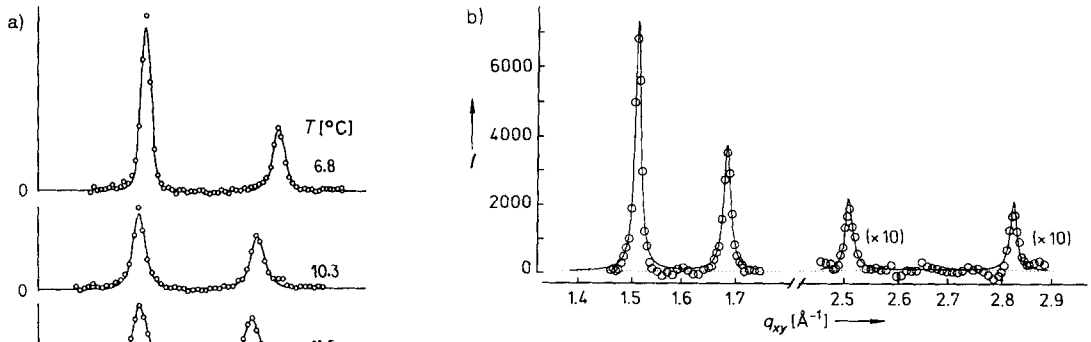

Fig. 20. a) GID data for a monolayer of the alcohol $C_{21}OH$ over pure water (from reference [35]) taken along the isobar at 30 mN m^{-1}. The peak intensity increases with decreasing temperature. The peak splitting is due to the transition from a hexagonal to a distorted hexagonal net. A linear background has been substracted. b) GID data for a monolayer of the acid $C_{20}CO_2H$ over pure water (from reference [46]) at 5 °C and $\pi \approx 35$ mN m^{-1}. Under these conditions the diffraction spectra of the alcohol and the acid are identical. A linear background has been subtracted. In addition to the two reflections observed in a) for 6.8 °C, two higher order reflections are shown here with 10 × magnification.

3.3. Crystalline Self-Assembly of Noncompressed Monolayers

The degree of crystalline order in biological lipid membranes in solution is probably low. But we may expect a high degree of order in self-aggregated clusters of amphiphilic molecules at the water surface because of the constraints imposed: a "flat" surface and solvent in contact only from the hydrophilic side. Direct evidence is now available from GID, but only for water-insoluble species. For soluble species, characterization by X-ray diffraction has not yet been achieved, possibly because of the low scattering power of these molecules. In addition, the range of crystallinity of the clusters may be very small. Nevertheless, evidence for aggregation comes from specular reflectivity data;[53] evidence for some degree of ordering comes from oriented epitaxial crystallization in the subphase at the solution surface.[5] More recently a remarkable observation was made by fluorescence microscopy:[54] two-dimensional faceted crystals of sodium dodecyl sulfate with sides of the facets as long as 50 μm could be seen on the water surface for a concentration of 0.055% by weight, which is far below the critical micelle concentration (0.25% by weight). For water-soluble surfactants, only reflectivity measurements yield structural information on the molecular level, which we now describe in some detail.

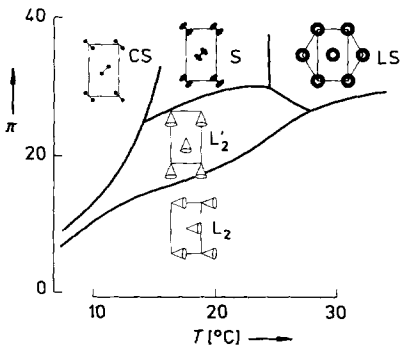

Fig. 21. π–T phase diagram of docosanoic acid ($C_{21}CO_2H$, also called behenic acid) monolayers over pure water. See text for an explanation of the structures.

Neutron reflectivity measurements (Fig. 22a) performed on a soluble surfactant, decyltrimethyl ammonium bromide (DTAB) at the air–solution interface[53] provide some information on the self-organization of the system. They indicate a vertical alignment of DTAB molecules, yielding a layer thickness of about 16 Å for concentrations varying from 0.002 to 0.01 M. Since the extended chain plus head group is about 17 Å thick, the molecules are assumed to lie in one layer as shown in Figure 22b. At a concentration of 0.05 M, where the monolayer is essentially complete, the reflectivity measurements yielded a film thickness of about 21 Å. This was explained in terms of a staggered arrangement reducing the electrostatic repulsion (Fig. 22b, bottom).

X-ray reflectivity measurements of norleucine solutions and surface tension measurements of several hydrophobic α-amino acids (for example, leucine, valine, isovaline, phenylalanine) and α-amino octanoic acid suggested accumulation of the molecules at the air–water interface.[5] Concrete evidence for organized 2D clusters of these molecules at the air–water interface was obtained by crystallization experiments:[5] they promote formation of α-glycine crystals at the water surface and growth through specific faces. The occurrence of these faces can be controlled by choosing the additive; thus a direct correlation is established between organized aggregates of the hydrophobic α-amino acid at the surface and the face of α-glycine through which the crystal grows.

If these short-chain hydrophobic α-amino acids spontaneously aggregate at the interface, Langmuir monolayers such as palmitoyl-lysine (PL) and "perfluoro"aspartate (PFA), which also induce α-glycine crystallization, should behave similarly. PL in the uncompressed state at room tem-

perature did not yield any diffraction signal.[25] But uncompressed PL with an average molecular area 10–15 times greater than its molecular area in the compressed state induced oriented crystallization of α-glycine, suggesting ordered monolayer domains.[3b, 3c] Apparently these domains at room temperature are too low in coherence length to be detected by surface diffraction. In contrast, as mentioned earlier, self-assembled crystalline domains of PFA were detected by GID with only 50% surface coverage. The fluorine

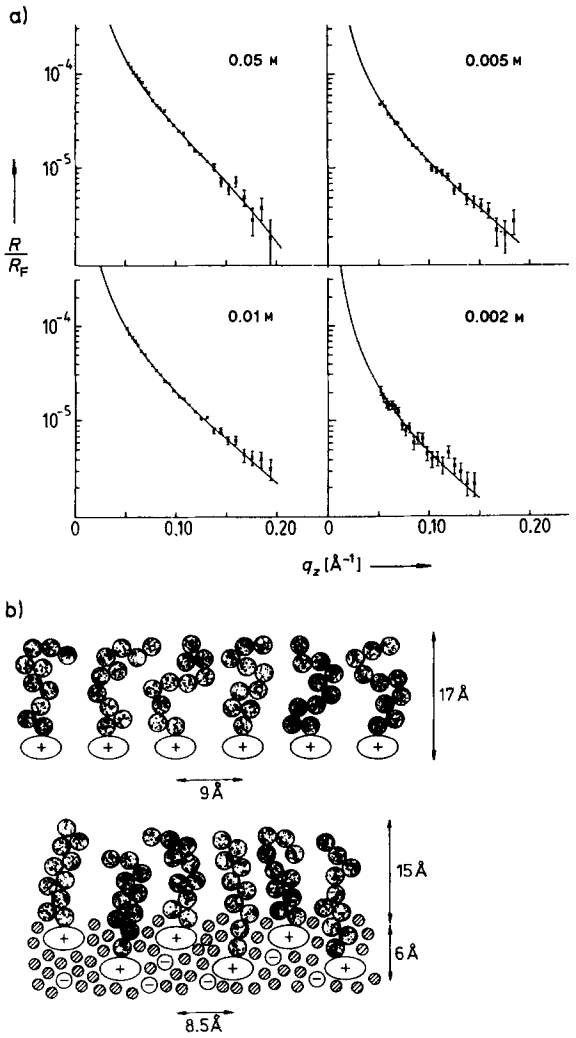

Fig. 22. a) Observed neutron specular reflectivity profiles of fully deuteriated DTAB in contrast matched water, for different concentrations, and the theoretical model fitted thereto ([53a]). b) Model for the distribution of water and DTAB ions at the air–solution interface. Top: Configuration of the molecules within the adsorbed layer at concentrations of 0.01 M or less. Bottom: The surface layer at 0.05 M, deduced from isotopic substitution neutron measurements ([53a]). ◉ = CH_2 and CH_3 of the carbon chain, ◎ = water molecules, ⊕ = head group $+N^+-CH_3$).

atoms, which induce a helical conformation in long fluorocarbon chains,[55] render these chains stiffer than aliphatic hydrocarbon chains and lower the possibility for conformational disorder. Hence, Langmuir monolayers of fluorinated molecules were characterized by a higher crystallinity than their hydrocarbon counterpart. GID data of fluorinated monolayers of PFA[30a] and $C_{10}F_{21}CH_2CO_2H$[56] suggested the coexistence of crystalline and dilute disordered phases; in dilute phases the PFA molecules have a molecular area of about 100 Å^2 and $C_{10}F_{21}CH_2CO_2H$ molecules an area of 2000 Å^2, indicating a gaseous state. This result may be compared with results obtained for arachidic acid monolayers ($C_{19}CO_2H$) at room temperature and at low surface pressure[47] where in the tilted solid phase the molecular area is 24 Å^2; this phase coexists with a fluid phase of molecular area 31 Å^2.

Lowering the temperature has considerably enhanced the tendency for high crystalline order in the uncompressed state, presumably by reducing molecular motion and so enabling effective intermolecular interactions. Low temperature GID studies were performed on several monolayers C_nX with different head groups X, such as $C_{23}OH$, $C_{30}OH$, $C_{31}OH$, $C_{29}CO_2H$, $C_{19}CONH_2$, and $C_{19}CONHC_2H_4CO_2H$. The probable packing characteristics of these spontaneously formed crystallites were extracted from the GID data.[48] We present here a brief description of the packing arrangements of the alcohols (X = OH), the acid (X = CO_2H) and the amide (X = $CONH_2$) monolayer. These packings were deduced by taking advantage of the known 3D crystal structures of molecules with long hydrocarbon chains. This strategy is meaningful since these 3D structures can be described as stacks of layers of molecules; thus the molecular arrangement in a single layer may well resemble that of the monolayer.

Long-chain alcohols and acids possess layered 3D crystal structures. In each layer the molecules are related by a glide so that neighboring hydrocarbon chains have parallel mean axes, but are in a mutually perpendicular orientation when viewed down the mean axis; the arrangement is described as orthorhombic orthogonal.[52] Common to all these structures are the parameters of the orthorhombic subcell, which is a projection of the unit cell onto a plane perpendicular to the molecular axis.[52] The subcell may be regarded as rectangular with dimensions $a_s = 4.98$, $b_s = 7.42$ Å, corresponding to a cross-sectional area of 18.48 Å^2. Remarkably, the calculated 2D cells of the monolayers projected onto a plane perpendicular to the molecular axis perfectly match the orthorhombic subcell of the 3D crystal structures. Following this observation and the diffraction data analysis, it was deduced that the alcohol and the acid monolayer molecules appear in the orthorhombic orthogonal packing, that is, they are related by a glide in a primitive rectangular cell as shown in Figure 23a and 23b. In this arrangement, the hydrogen atoms of adjacent hydrocarbon chains intermesh, thus ensuring close packing of the chains.[52] Further, the molecular chain axis is parallel to the glide plane so that intermolecular contacts between methylene CH_2 groups of the glide-related molecules are the same along the chains.

In 3D crystal structures of long-chain primary amides,[57] the interactions between the molecules are controlled by a network of hydrogen bonds at the $CONH_2$ head groups. The same feature applies to the motif proposed for the monolayer crystallites. The chains are stacked by translation with the molecular axis tilted at an angle of 18° to the normal to the *ab* plane (which is parallel to the water surface) in the direction of the 4.69 Å translation axis (Fig. 23c). The molecules are related by translation in a *c* centered rectangular cell. Thus, the monolayer space group is *c*1. The exact molecular orientation is determined by the fact that the $CONH_2$ amide

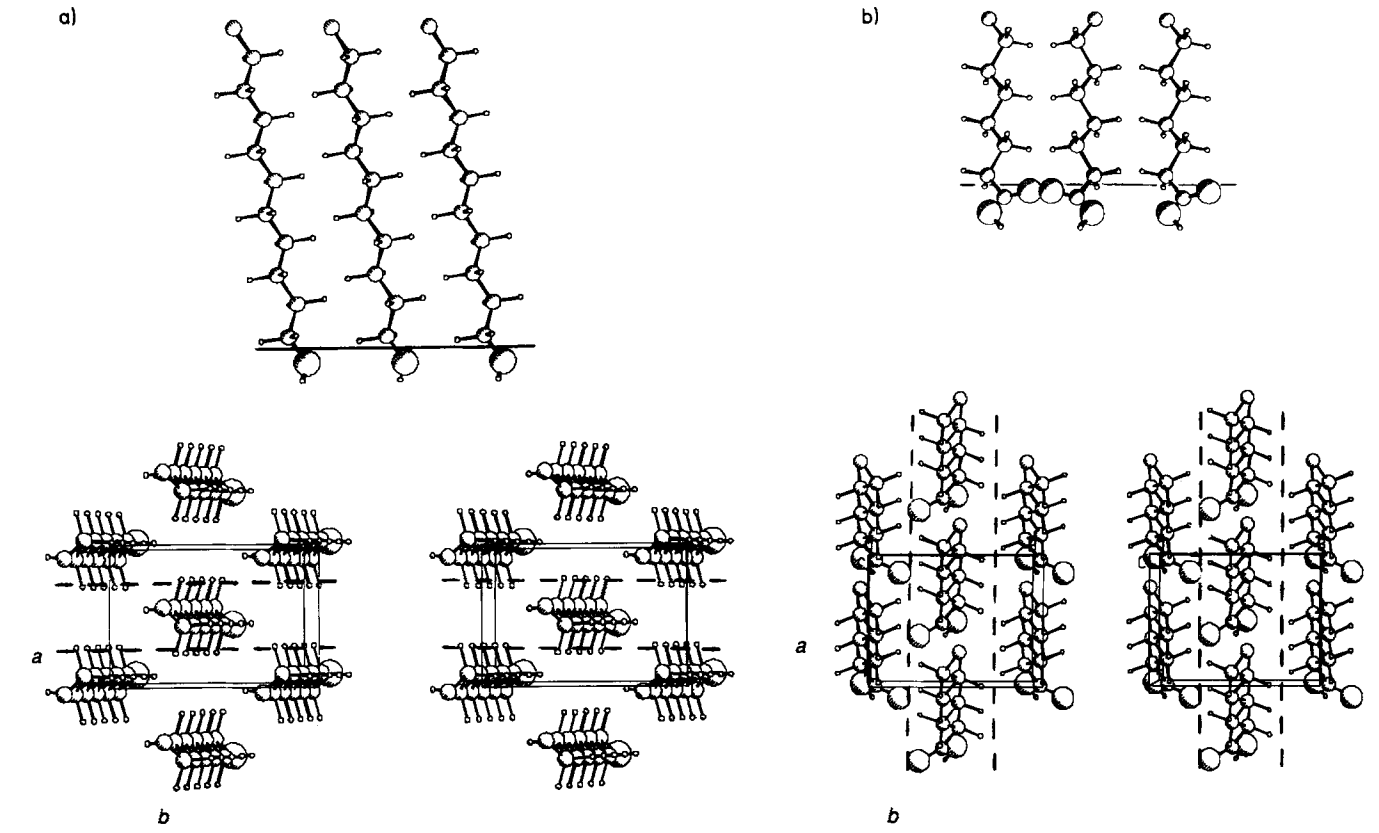

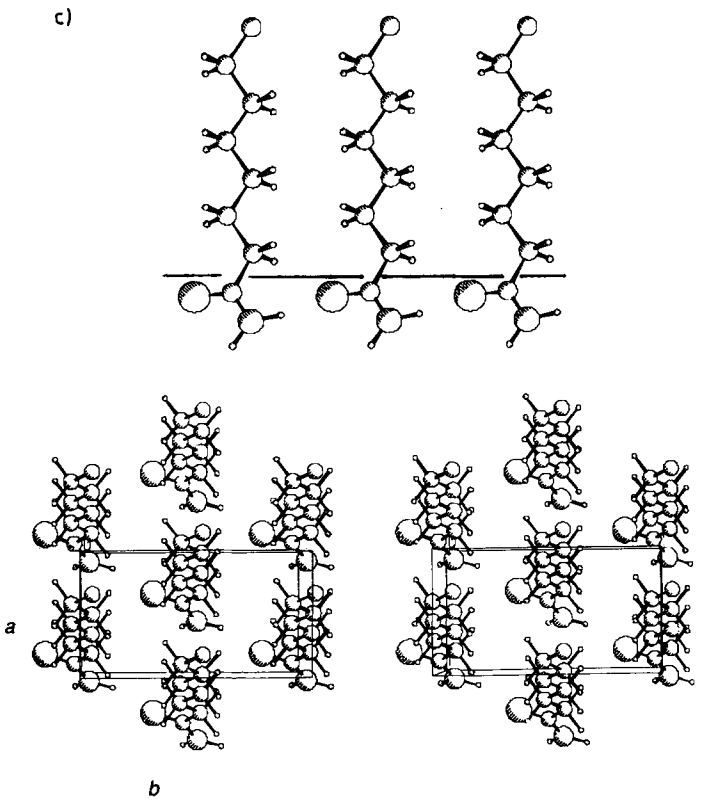

Fig. 23. Models of the hydrocarbon chain packing in the alcohol, carboxylic acid, and amide crystallites formed at 5 °C over pure water. Bottom: Stereoscopic view of the packing arrangement, seen perpendicular to the water surface; top: a side view along a direction parallel to the water surface (indicated by a solid line). For clarity only the head group and maximally eleven methylene groups CH_2 of each molecule are shown. On the last carbon atom drawn the hydrogen atoms are omitted. The rectangular cell (*a*,*b*) is indicated. The glide symmetry elements, when present, are shown as dashed lines. For convenience the origin of the unit cell is placed halfway between adjacent glide planes. a) Alcohol monolayers ($n = 23, 30, 31$). Since the molecules are tilted along the *b* axis ($t = 9.5°$), the projected cell down the mean molecular axis onto the water surface is given by $a_s = 4.99$ Å, $b_s = 7.53$ Å $\cos 9.5° \approx 7.43$ Å. b) Triacontanoic acid monolayer C_nCO_2H ($n = 29$). Since the molecules are tilted along the *a* axis ($t = 26.8°$), the projected cell down the mean molecular axis onto the water surface is given by $a_s = 5.53$ Å $\cos 26.8° \approx 4.94$ Å, $b_s = 7.44$ Å. c) Arachidamide monolayer ($n = 19$). Here $t = 18°$, $a = 4.69$, $b = 8.69$ Å.

groups form NH · · · O hydrogen bonds parallel to the diagonal (**a** ± **b**) (Fig. 23c).

The positional correlation lengths of all the crystallites were found to be anisotropic;[48] they extend over only 35 to 95 spacings parallel to the molecular tilt direction, but over 135 to 270 spacings perpendicular to it. These results suggest that the monolayer crystallites are strips elongated perpendicular to the molecular tilt direction. The same observation was made in the L_2 phase of behenic acid[47] (cf. Fig. 21 and the related discussion). It would be interesting at this point to understand the relationship between the amphiphilic structure and the monolayer crystal morphology.

4. Influence of Ions and Solutes on Monolayer Organization

4.1. Solute Binding and Its Effect on Growth and Dissolution of Monolayers

The binding of solute molecules to hydrophilic groups of monolayers allows us not only to probe the solutes effect on the growth, stability, and dissolution of 2D crystals, but also

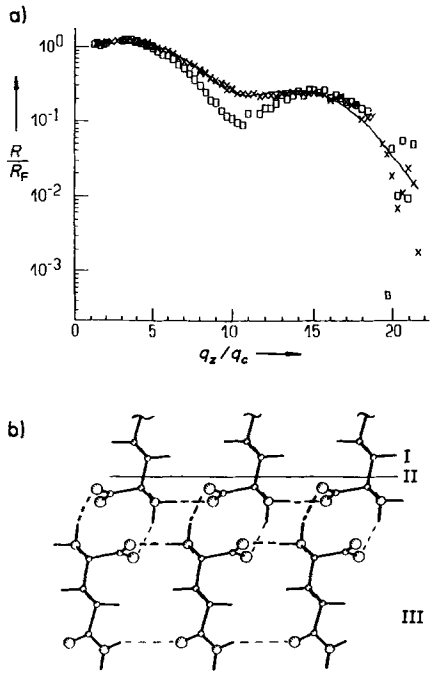

Fig. 24. a) Reflectivity data of compressed monolayers of (*R*)-PL over water (□) and over an unsaturated solution of (*S*)-glutamine (0.137 M, ×). b) A model of surface enrichment of glutamine at the interface (II). Only a short segment of the hydrophobic chains (I) are represented. Hydrogen bonding (– – –) between amide groups of neighboring glutamine molecules, and between the glutamine layer (III) and the monolayer is shown.

to simulate interactions between the surface of a 3D crystal and solvent or solute molecules.

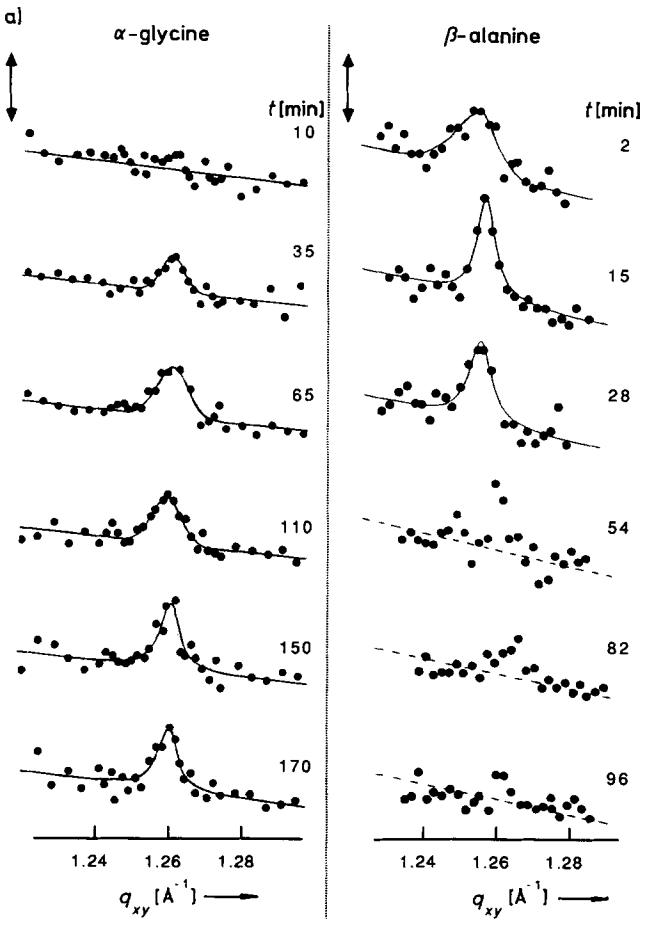

To date it has not been possible to monitor the process of nucleation and crystallization of layered 3D structures such as α-glycine or other amino acids from the air–water interface. But it is possible, with unsaturated solutions of these compounds, to show that the solute binds to the monolayer in a way that mimics the formation of the nucleating crystal's first layer. Indeed, XR studies showed that even in unsaturated solutions of amino acids, the solute molecules bind to the interface. Reflectivity measurements were made on monolayers of PL over a dilute aqueous solution of glutamine $NH_2COC_2H_4CH(NH_3^+)CO_2^-$.[40] Advantage was taken of the possibility that glutamine may bind to the monolayer through NH···O bonds as well as to neighboring glutamine molecules by NH···O (carboxylate) and NH···O=C (amide) hydrogen bonds (Fig. 24b). The reflectivities of a monolayer of palmitoyl-(*R*)-lysine over the solution or over pure water are quite different (Fig. 24a). Analysis of the two data sets shows that as many as a quarter of the sites below the head groups are occupied by glutamine. The result is in qualitative agreement with the model shown in Figure 24b.

Addition of a solute to the subphase can deter crystalline self-aggregation of monolayers, allowing its growth to be monitored as a function of time. The left part of Figure 25a shows that 10 minutes after a PFA monolayer was deposited over an unsaturated solution of α-glycine, no diffraction peak was observed. This is in contrast to the observation made when PFA was deposited over a pure water subphase.[30] It took around 30 minutes before crystalline domains could be detected. This inhibition can be understood from the top part of Figure 25b, which shows how one glycine molecule can bind to two neighboring molecules of the α-amino acid monolayer with very strong hydrogen bonds, hindering their assembly. The formation of this complex is in kinetic competition with that of the crystalline

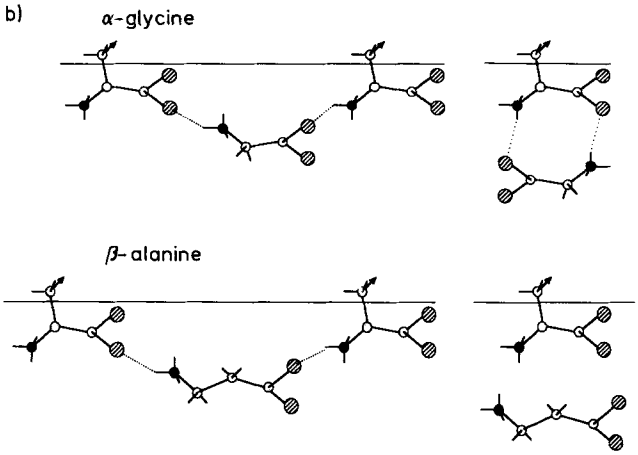

Fig. 25. Uncompressed monolayer ($\pi = 0\ mN\,m^{-1}$) of PFA with an average molecular area of 45 Å^2 over various solutions. a) GID measurements as a function of time after spreading. Left: Over α-glycine solution (0.015 M). Right: Over β-alanine solution (0.005 M). Note the increase in crystallinity in the former, and the decrease in the latter as indicated by the different time evolution of the peak. The length of the double-sided arrow represents 200 counts. b) Left: Schematic drawings of "bridging complexes" between PFA monolayer molecules and the solute molecules for α-glycine (top) and β-alanine (bottom). Right: A potential quasidimer is illustrated for α-glycine, while the mismatch is depicted for β-alanine. ◍ = O, ○ = C, ● = N, – – – = hydrogen bonds, → = hydrophobic chains.

hydrogen-bonded bilayer which is composed of quasi-cyclic dimers of PFA and α-glycine (Fig. 25b, top right). That this bilayer is eventually formed is deduced from the following observations: firstly, glycine forms oriented crystals attached to monolayers of PFA, denoting formation of a bilayer at the onset of crystallization;[3] secondly, monolayers of PFA over glycine solutions maintain their crystallinity after compression and decompression, unlike PFA over pure water;[30b] finally X-ray reflectivity measurements of monolayers of PL over glycine solutions showed that the glycine molecules accumulate at the interface,[40c] which is indirect evidence for the formation of an incomplete bilayer, as in the experiment with glutamine.

Use of β-alanine NH_3^+-CH_2CH_2-CO_2^- instead of glycine as a solute molecule had an entirely different effect on the 2D crystals of uncompressed PFA; this amino acid did not strongly inhibit growth, but caused a complete dissolution of the PFA crystals within two hours as shown by GID measurements (Fig. 25a, right). This dissolution can be rationalized in terms of a strong interaction of β-alanine with the amino acid head groups of adjacent surfactant molecules leading to a disruption of the 2D crystal (Fig. 25b, bottom). It is noteworthy that because of a molecular mismatch, β-alanine can hardly form a hydrogen-bonded cyclic dimer with the amino acid head group of the monolayer and certainly not a hydrogen-bonded counterlayer commensurate with the monolayer, as can glycine (Fig. 25b, bottom).

4.2. Ion Binding from Solution

The interfacial region between a charged surface and an electrolyte is central to many processes such as those occurring during electrodeposition, ion transport through biological membranes, preparation of Langmuir–Blodgett films,[6] biomineralization,[4] and induced oriented nucleation of inorganic systems[3c, 3d] under Langmuir monolayers. X-ray reflectivity measurements demonstrated that metal ions in the solution interact closely with the charged monolayer head groups at the interface.[28, 58] However, it was still an open question whether the ion distribution near such charged, ordered surfaces was crystalline. In a recent study,[24b] the interface between a phospholipid monolayer and a $ZnCl_2$ aqueous solution was measured with X-ray standing waves. The technique, described in Section 2 is sensitive to the ion distribution normal to the surface and allows the distinction between a vertically nondiffuse ionic layer (Helmholtz model) and diffuse ionic layers (Gouy–Chapman and Stern models). It was concluded that the double layer at the phospholipid membrane–aqueous interface is diffuse along the

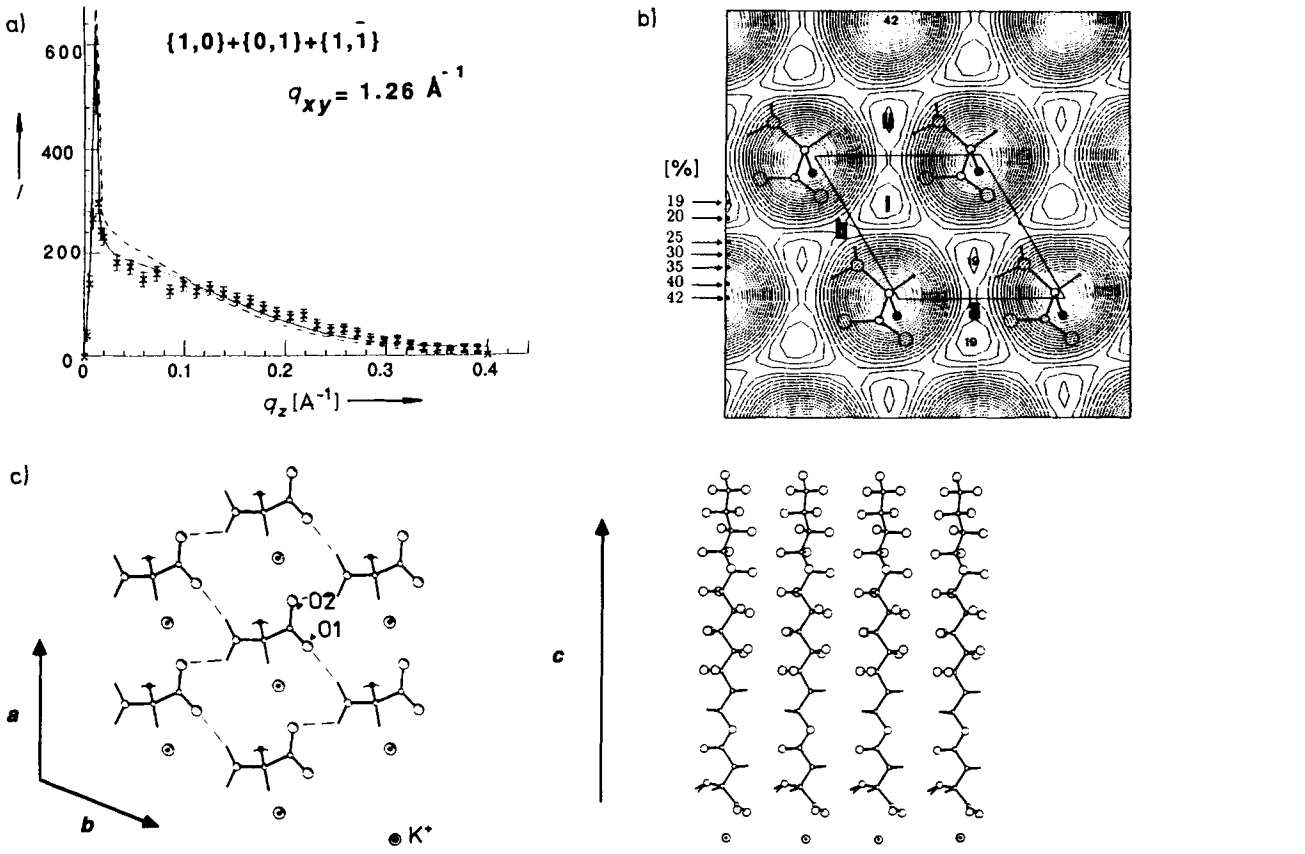

Fig. 26. Uncompressed PFA monolayers over KOH subphases (pH = 11.5; room temperature; π = 0 mN m^{-1}). a) Bragg rod scan measured on the GID peak (whose reflection assignment and position is indicated) with a calculated fit including (solid line) and excluding (dashed line) the contribution of K^+ ions. b) *R*-factor contour map (interval 1%), which expresses the fit between the calculated and observed data, obtained from BR fits as a function of the lateral position of the K^+ ion in the PFA hexagonal unit cell at a fixed *z* coordinate. The two sites with the lowest *R* factors (19%) labeled I and II are potential sites for the K^+ ion. The model (Fig. 26c) favors site I for the K^+ ion. c) Model of the uncompressed monolayer of PFA over K^+ ions. Left: View along the *c* axis (perpendicular to the monolayer) showing the hexagonal net of K^+ ions bridging the oxygen atoms O1 and O2 of two neighboring molecules. Right: View along the *a* axis showing the attached layer of K^+ ions (water molecules possibly interleaved in the ionic layer are not shown here).

normal to the film. GID measurements of lead–arachidate[59] monolayers at room temperature did not demonstrate the existence of laterally ordered or nondiffuse layers of Pb^{2+} counterions. Liquid surface EXAFS experiments on manganese–stearate films[22] at room temperature yielded a Mn–Mn nearest neighbor distance at the surface in the compressed phase only, indicating at least short-range order.

A weak indication of lateral order of ions is provided by GID data of uncompressed monolayers of PFA over a HCl solution[30a] at a pH of 1.5. A model was proposed in which the Cl^- ions were partially intercalated between neighboring NH_3^+-CHR-CO_2H sites, participating in attractive $NH^+ \cdots Cl^-$ and $COH \cdots Cl^-$ interactions. This model also explains the high molecular area of 31.6 Å^2, compared to the value of 28.5 Å^2 over basic subphases (discussed below), which imposes a tilt of the molecule of 25° from the vertical according to the GID data. The model is also in keeping with the observation that in 3D crystals of glycine · HCl, the molecules appear in a layered arrangement with intercalated Cl^- ions.[60]

PFA monolayers on highly basic KOH subphases (pH = 11.5) yielded results favoring a laterally ordered bilayer.[30a] The presence of the K^+ ions induces all molecules to be assembled into crystals even in the uncompressed state, with the molecules aligned vertically in a hexagonal cell. According to an analysis of the GID data (Fig. 26a,b), the K^+ ions occupy ordered sites bridging oxygen atoms of adjacent molecules (Fig. 26c). The XR measurements on compressed monolayers at high pH over KOH indicate excess electron density just below the head group. This excess density is consistent with one K^+ ion and one H_2O molecule per head group. Upon compression, lateral pressure introduces defects in the randomly oriented islands, causing a reduction in crystallinity. It is possible that the distortion occurs at the periphery of the crystallites due to strong electrostatic interperipheral forces between anion–cation bilayers of neighboring crystallites. It is noteworthy that in both systems, PFA over acidic and basic subphases, the counterions retain the original molecular packing and a long-range crystalline order is maintained after decompression. This is in contrast with results for films over pure water.[30a]

As mentioned earlier, lowering the temperature has the effect of reducing molecular rotational disorder and enhancing crystalline self-aggregation. Indeed, a GID study of uncompressed cadmium arachidate monolayers over a subphase with its pH adjusted to 8.8 with ammonia demonstrated the presence of an ordered Cd^{2+} layer[61] with a coherence length of 1000 Å at temperatures lower than 9 °C. The diffraction spectrum showed ten distinct peaks (Fig. 27), seven of which were attributed to the Cd^{2+} layer. The remaining three peaks were deduced to stem from the arachidate layer, on the basis of their Bragg rod profiles and q_{xy} positions. The diffraction peaks of the Cd^{2+} lattice, whose BR profiles were flat and extended, indicative of a thin monoatomic layer, could be indexed according to a 2 × 3 supercell of the arachidate cell. Such a supercell demands three cadmium ions, given a 1:2 molar ratio of cadmium ions to acid molecules. The two lattices are shown in Figure 27c. The calculated diffraction peaks due to the refined positions of three Cd^{2+} ions in the supercell are shown in Figure 27b. In contrast to films of cadmium arachidate, a film of calcium arachidate

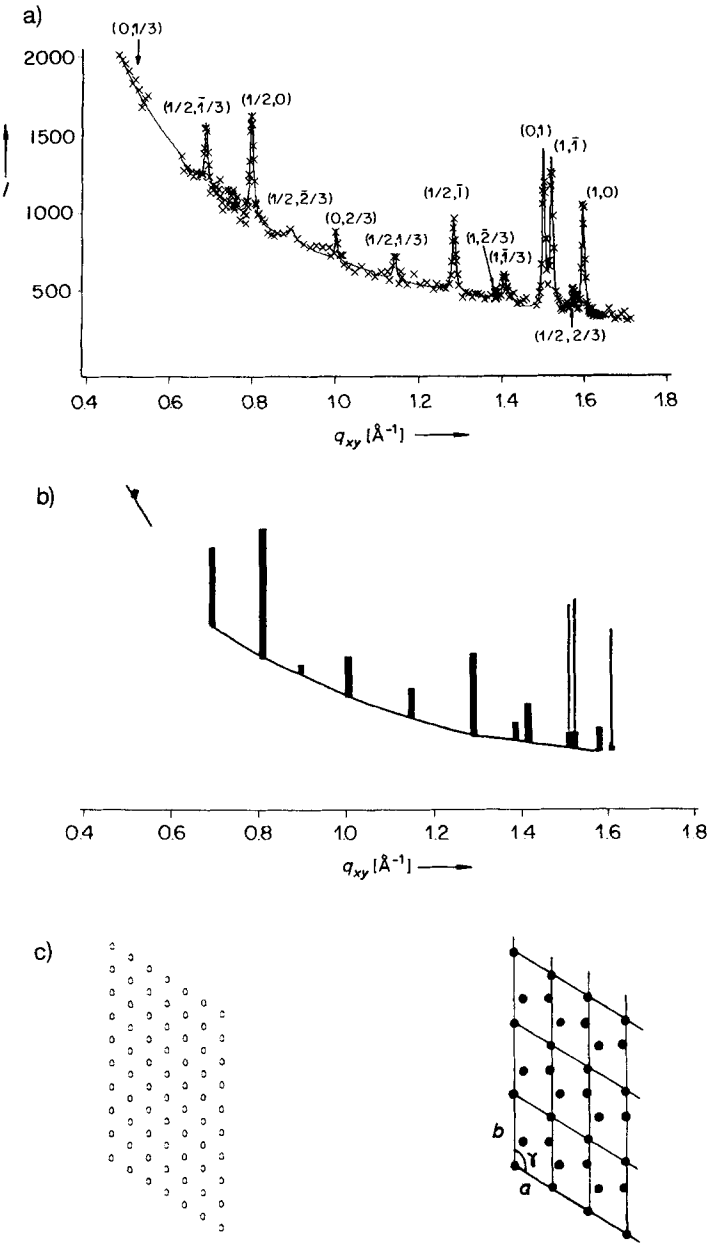

Fig. 27. Arachidic acid monolayer ($C_{19}CO_2H$) over a 10^{-3} M $CdCl_2$ subphase (pH = 8.8) in the uncompressed state (π = 0 mN m^{-1}) and at low temperature (9 °C). a) GID peaks and assignment of reflections. Reflections with integer indices correspond to scattering arising from arachidate moities, and those with fractional indices to scattering from a 2D layer of Cd^{2+} ions. b) Calculated powder pattern for the cadmium net superimposed on background scattering. The peaks labeled with thin lines are the arachidic triplet. c) Two-dimensional lattices of arachidate (left) and cadmium ions (right). The cadmium cell is a 2 × 3 supercell of the arachidate cell. The positions of the Cd^{2+} ions in the cell are marked as filled circles.

over water at low temperatures did not provide direct evidence for an ordered Ca^{2+} layer.[62] Nevertheless, the Ca^{2+} ions did induce high crystallinity of the uncompressed phase at high pH; the molecules were aligned vertically. These results agree with the conclusions of a recent surface-potential and surface-pressure study of ionic interactions with fatty acid monolayers:[63] whereas monolayer ordering is induced by covalent binding between carboxylate (CO_2^-) and metal ions in the case of Cd^{2+}, Ca^{2+} ions do not exhibit such an ordering effect because their interactions with carboxylates are mainly ionic in nature. The adsorption of ions at the

monolayer molecules and the resulting structural variations in the monolayer were also studied recently by GID.[64] The structural changes in henicosanoic acid monolayers induced by the introduction of Cu^{2+} or Ca^{2+} ions into the subphase were investigated.

5. Transfer of Structural Information from Langmuir Monolayers to Crystals

Langmuir monolayers have been shown to induce oriented crystallization from solution of proteins[65, 66] and other organic and inorganic compounds.[3] As mentioned in the introduction, these studies were motivated by their revelance to crystal nucleation, to two-dimensional ordering at the water surface of soluble hydrophobic molecules, and to biomineralization. The crystal systems studied to date include α-glycine,[3a] sodium chloride,[3c, 3d] calcium carbonate,[4a-d] parahydroxybenzoic acid,[67], hexagonal ice,[68] barium sulphate,[69] and silver propionate.[70] Mechanisms for crystallization through particular faces (oriented crystallization) involve structural fits and electrostatic attractions. Information on the monolayers used and the type of crystal face nucleated are listed in Table 2 for some of these crystal systems.

5.1. Inorganic Crystals and Biomineralization

Electrostatic interactions between Langmuir monolayers and crystals have been invoked to account for the oriented growth of inorganic salts. A first example is given by the oriented nucleation of NaCl crystals under α-amino acid monolayers such as PFA. NaCl precipitates from aqueous solution in a cubic cell ($a = 5.64$ Å) exhibiting six (100) faces. But when crystallized under α-amino acid monolayers at pH ≈ 7, crystals were found to be attached to the monolayer by the less stable (110) face (Fig. 28a).[3d, 30] This face is composed of alternating rows of Na^+ and Cl^- ions, separated by 2.82 Å. This distance is very close to the separation of 2.8 Å between rows of NH_3^+ and CO_2^- moieties in PFA. Thus we envisage an electrostatic attraction between small domains of a (110) surface layer of NaCl and the zwitterionic α-amino acid head groups of PFA at pH ≈ 7. At high pH (>10), PFA monolayers induce crystallization of NaCl from the metastable (111) face. A pure (111) face of NaCl exposes a singly charged layer consisting entirely of either Na^+ or Cl^- ions (Fig. 28b). This selectivity was explained in terms

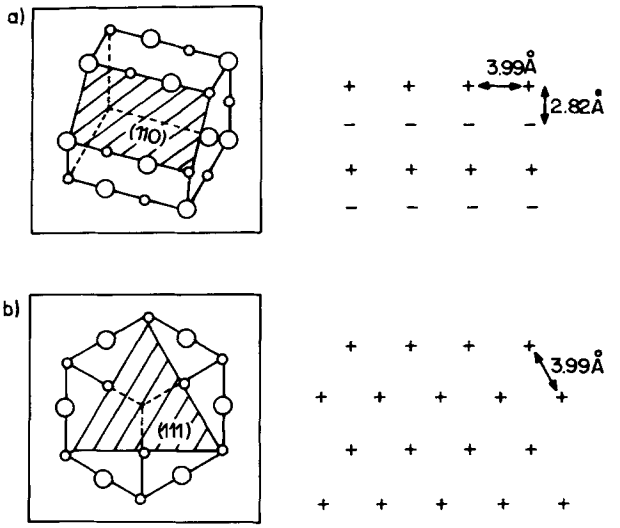

Fig. 28. Schematic representation (left) and point charge distribution (right) of faces of a NaCl crystal. a) The (110) face. b) The (111) face. ○ = Na^+, ○ = Cl^-.

of a simple electrostatic interaction between the CO_2^- charged monolayer surface and an underlying layer of Na^+ ions which induces a homogeneous surface potential for (111) nucleation. The lattices of the PFA monolayer and the (111) layer are not similar. There is a possibility of interleaving ordered water in the first attached layer of Na^+ ions, which could play a role in inducing oriented nucleation of the (111) face since OH groups can form OH···Cl^- hydrogen bonds with Cl^- ions in the second layer.[60]

As mentioned earlier, GID results on PFA monolayers over HCl solution at low pH was interpreted in terms of a partial intercalation of Cl^- ions within the head-group layer.[30] Thus, rows of positive (NH_3^+) and negative (Cl^-) charges are created at the surface, simulating the repeat mo-

Table 2. 3D crystals induced by monolayers at the air–water interface

3D Crystal	Monolayer[a]	Nature of Binding	Crystal Face	Ref.
NaCl	acids and α-amino acids			
High pH	RCO_2^- H_2N-CHR-CO_2^-	electrostatic binding, no match	(111) metastable charged face	[3c–d], [30a]
Neutral pH	$H_3\overset{+}{N}$-CHR-CO_2^-	electrostatic binding, partial match	(110) face, less stable than normal (100)	
$CaCO_3$	acids RCO_2H amines RNH_2	electrostatic binding, partial match for calcite	Calcite: (1$\bar{1}$0) face, vaterite: (0001) face Vaterite: (0001) and (110) faces	[4a–d]
α-Glycine $H_3\overset{+}{N}$-CH_2-CO_2^-	α-amino acids $H_3\overset{+}{N}$-CHR-CO_2^-	NH···O hydrogen bonds, structural match	(010) chiral face, not well developed in H_2O	[3]
Para-hydroxybenzoic acid monohydrate HO_2C-C_6H_4-OH + H_2O	alkoxybenzoic acid HO_2C-C_6H_4-OR	interlayer contacts induce a structural match	(401) face, not well developed in H_2O	[67]
Ice	alcohols ROH	OH···O hydrogen bonds, lattice plus structural match	(0001) hexagonal face	[68]

[a] R is a long chain alkyl group of general formula C_nH_{2n+1}.

tif of the charge distribution in the (110) face. Indeed, at low pH, NaCl crystallizes from its (110) face attached to the PFA monolayer.[30]

The influence of structured organic surfaces on oriented growth has a strong bearing on biomineralization.[*] Addadi, Weiner, and co-workers[4e] have studied the effect of β-pleated sheet proteins on crystallization of calcite. They demonstrated oriented calcite nucleation probably arising from a combination of electrostatic and structural requirements. To elucidate this result on a molecular level, Mann and co-workers studied the induced oriented crystallization of $CaCO_3$ under monolayers of stearic acid[4a, 4b] and other amphiphiles such as amines.[4c, 4d] Whereas crystallization of $CaCO_3$ in the absence of a monolayer of acid or amine results in rhombohedral calcite crystals, the stearic acid monolayers give rise to oriented nucleation of the less stable hexagonal polymorph of vaterite from the (001) face. We present here a model for the interface, based on the crystallization results of NaCl below a monolayer and the structural data of cadmium arachidate and calcium arachidate monolayers. The double layer comprising the stearic acid molecules and the calcium ions must be neutral, implying a 2:1 stochiometry as confirmed by X-ray and neutron reflectivity studies of the fatty acids over $CaCl_2$ and $CdCl_2$ solutions.[28, 58] Thus the repeat area per Ca^{2+} ion must be twice that of the stearic acid molecule. As mentioned earlier there is as yet no direct evidence of order in a layer of Ca^{2+} counterions. The density of such a Ca^{2+} layer is low and we may assume at least one to two interleaving water molecules per Ca^{2+} ion, which is consistent with X-ray reflectivity data.[28, 62] The water molecules would screen neighboring Ca^{2+} ions and form $OH\cdots O$ hydrogen bonds with the monolayer carboxylate groups CO_2^- above and carbonate ions CO_3^{2-} below the Ca^{2+} layer (Fig. 29a). According to GID data of calcium arachidate,[62] the arachidate molecules stand up straight even in the uncompressed state. Thus, the orientation of the CO_2^- groups is similar to that of the CO_3^{2-} groups in vaterite.

The hydrogen-bonded $OH\cdots OCO_2^{2-}$ system tends to be coplanar as in the crystal structure of $Na_2CO_3 \cdot 3/2\ H_2O_2$.[80] This preference would promote bound carbonate molecules oriented perpendicular to the Ca^{2+} layer. Vaterite has a crystal structure with carbonates oriented in this way (Fig. 29b), while the orientation of the carbonates in the calcite structure is different. This may account for the preferred nucleation of vaterite.

An alternative model for the preferential formation of vaterite involving an epitaxial relationship between the (001) face of vaterite and the 2D lattice of calcium stearate appears to be plausible since the *a* and *b* axes of vaterite are 7.15 Å, approximately 1.5 times the length of the *a* and *b* axes of the calcium arachidate monolayer. On such a basis, one may envisage a supercell common to both layers which is a 2×2 reconstruction of the vaterite lattice and a 3×3 reconstruction of the arachidate lattice. In such a cell, although the net charge brought in by the nine carboxylate groups is -9, the net charge brought in by the twelve calcium ions is $(+\ 24/2) = +12$ since each calcium ion contributes one charge to the neutralization of the carboxylate layer and one charge to the neutralization of the carbonate layer. There is no simple way to reconcile this charge difference.

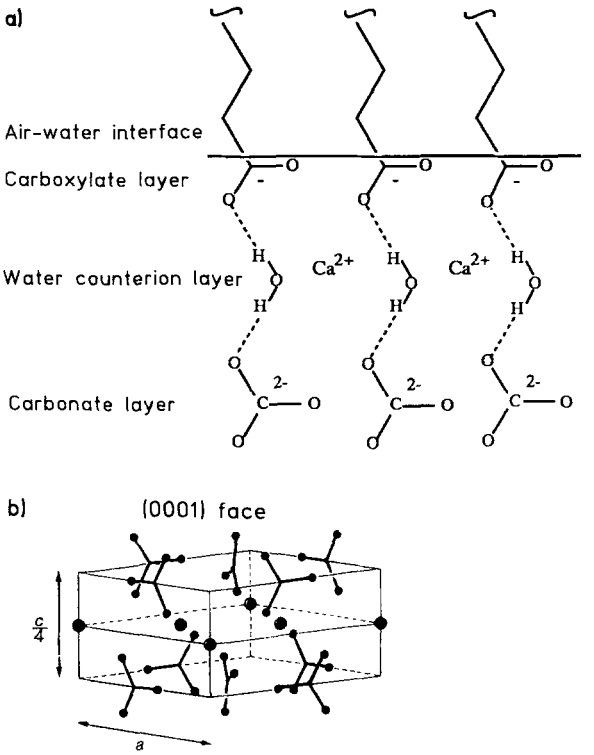

Fig. 29. a) Schematic representation of a calcium stearate monolayer, showing interleaved water molecules in the low density cationic layer which form hydrogen bonds with the carboxylate layer at the interface and with a carbonate layer in the subphase. In this layer the carbonate ions are oriented as in the (0001) layer structure of vaterite. b) Vaterite subcell showing the stereochemical arrangement of the carbonate ions perpendicular to the (0001) face (from [4a]). $a = 7.15$, $c = 17.00$ Å. ● = O atom, ● = Ca^{2+} ion.

5.2. Crystallization of Molecules under Monolayers with a Similar Head Group

An excellent structural fit between the head groups of the monolayer and the attached crystal layer is illustrated by the α-amino acid monolayer/glycine crystal system (Table 2). Glycine crystallizes in a bipyramidal habit (Fig. 30a) from aqueous solution in a monoclinic centrosymmetric arrangement. The glycine molecules form hydrogen-bonded layers (Fig. 30b). Such a layer may be easily replaced by a monolayer of resolved, chiral α-amino acid surfactant molecules provided the cross-sectional area of its hydrophobic chain is not larger than that of glycine (25.5 Å^2). Indeed glycine crystals grow stereospecifically from several α-amino acid Langmuir monolayers whose hydrophobic chains meet the above criterion.[3a, 3b] For example, the packing arrangement of the glycine head groups of the monolayer of PL, whose GID pattern[25] is shown in Figure 15, agrees very well with the layer structure of glycine.

The epitaxial crystallization of *para*-hydroxybenzoic acid (Table 2) under monolayers of *para*-alkoxybenzoic acid provides an example of how molecules in solution impose a change of monolayer structure probably at the onset of crystal nucleation. The *para*-hydroxybenzoic acid head groups of the monolayer change their orientation with respect to the

[*] Editorial comment: also in this issue is a review by L. Addadi and S. Weiner on "Control and Design Principles in Biological Mineralization".

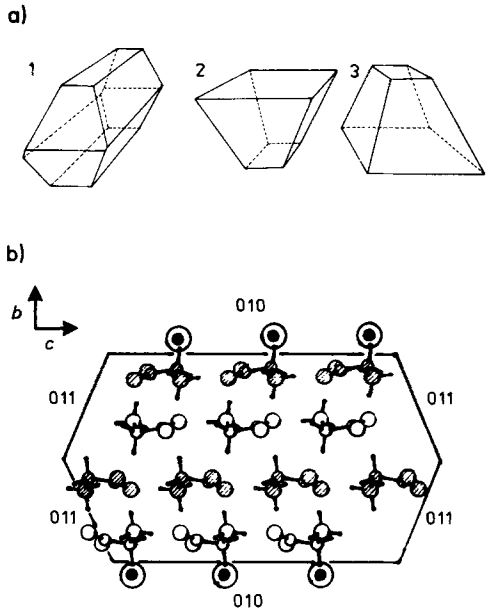

Fig. 30. a) Morphology of the pure α-glycine crystal grown from aqueous solutions (1) and at the monolayer solution interface (2 and 3). b) Crystal structure of α-glycine. An (*R*) α-amino acid monolayer induces the (010) face. An (*S*) α-amino acid monolayer induces the (0$\bar{1}$0) face. The hydrogen atoms of both faces are circled.

hydrocarbon chains so as to lie flat on the water surface, thus mimicking the (401) surface layer of the *para*-hydroxybenzoic acid crystal. It is noteworthy, as in the case of the α-glycine/monolayer system, that the crystals do not exhibit well-developed (401) faces in solution.

5.3. Nucleation of Ice by Monolayers

Pure water can be supercooled to temperatures as low as −40 °C. Therefore the induction or inhibition of the nucleation of ice, in particular through the role of auxiliaries such as membranes or proteins, has far-reaching ramifications for both the living and nonliving world. Promotion of ice nucleation has been exploited for the induced precipitation of rain by clouds seeded with silver iodide.[71] On the other hand, the promotion of ice nucleation by frost bacteria in crops can result in wide scale damage.[72]

Several mechanisms have been proposed to explain the promotion of ice nucleation such as a lattice or structural match between substrate and nucleated ice crystal[73] or an electric field present in the substrate, which orients the water molecules.[74] Experiments were conducted to design two-dimensional surfaces that raise the ice nucleation temperature. These experiments involved freezing of drops of water covered with monolayers of aliphatic alcohols (C_nOH) or carboxylic acids (C_nCO_2H). The structure of hexagonal ice[75] may be described for the oxygen atoms in terms of layers parallel to the *ab* plane where $a = b = 4.5$ Å, $\gamma = 120°$ (Fig. 31). Advantage was taken of the observation that at 5 °C uncompressed Langmuir monolayers of $C_{23}OH$, $C_{30}OH$ and $C_{31}OH$ over water pack in a distorted hexagonal net[48] ($a = b = 4.48$ Å, $\gamma = 113°$) that is similar in dimension to the *ab* lattice of hexagonal ice at 0 °C. The largest mismatch between the two lattices is 10% along the $a + b$ diagonal. The uncompressed monolayer of the carboxylic acid $C_{29}CO_2H$ has axial dimensions[48] $a = b = 4.6$ Å, $\gamma = 107°$. For this system the largest mismatch with ice is, once again, in the $a + b$ direction, but with a value of 27%. A structural similarity can be proposed for the OH head groups of the alcohol monolayer and the *ab* layer structure of ice; however, no such similarity exists for the corresponding carboxyl head groups of the fatty acid monolayer.

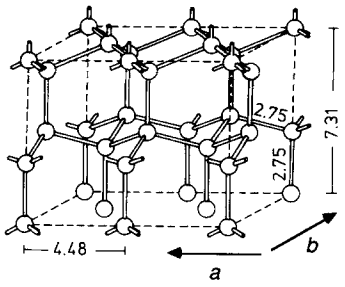

Fig. 31. Crystal structure of hexagonal ice (from [79]). The oxygen atoms of the water molecules are denoted by spheres and the disordered OH···O hydrogen bonds by rods. The hexagonal *a* and *c* axes are specified ($a = b = 4.48$, $c = 7.31$ Å).

The results of the ice nucleation temperature ("freezing point") measurements (Fig. 32) show that aliphatic chain alcohols are more efficient ice nucleators than the corresponding carboxylic acids.[68] Moreover, the freezing point

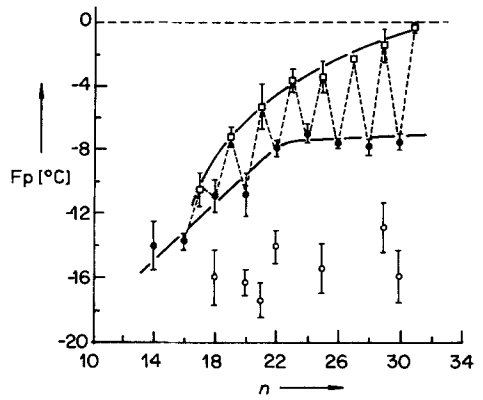

Fig. 32. Freezing points Fp of drops of supercooled water covered by monolayers of alcohols C_nOH (● = *n* even, and □ = *n* odd) and carboxylic acids C_nCO_2H (○). Freezing point curves are drawn separately for alcohols with *n* odd and *n* even. The error bars for each point were derived from 10 to 20 freezing point measurements.

is sensitive not only to chain length but also to chain parity (i.e., *n* odd or even) of the alcohol $C_nH_{2n+1}OH$ (Fig. 32). This trend suggests that at the temperature of ice nucleation the orientations of the alcohol OH groups in the odd and even analogues are not the same.

6. Outlook

The study of structures at interfaces has received an enormous boost with the recent development of surface X-ray diffraction methods using synchrotron radiation. Research in the crystallography of thin organic films should encompass a variety of exotic projects. For example, so far all the studies have been directed towards amphiphilic molecules bearing long hydrocarbon or fluorocarbon chains. With the

present advances in synchrotron techniques, it may soon be possible to obtain diffraction spectra from water-soluble amphiphilic molecules. Experimental results from oriented crystallization, chemical reactivity, and spectroscopic measurements suggest that molecules such as short chain α-amino acids, benzoic acids, or cinnamic acids form ordered clusters at the air–water interface.[5, 76]

The X-ray methods should allow one to test for the presence of lateral crystalline order in monolayers consisting of a collection of molecules engineered to construct a designed and well-defined lattice. Thus, these methods are intimately linked to the development of techniques to control and perfect the structure of Langmuir films on the molecular level. Perhaps we shall obtain a deeper insight into chemical transformation at the air–water interface by correlating the packing structure of reactant and product. An example of the latter is the topochemical photopolymerization of diacetylenes in monomolecular layers as studied by Göbel and Möhwald.[77] Another natural extension of these studies is the investigation of packing arrangements of amphiphilic molecules at organic solvent–water interfaces, as in emulsions. In such a system, the surface created by terminal groups of the hydrophobic chains makes van der Waals contacts with the organic solvent similar to those found for an alkane in a bilayer membrane.

The X-ray methods should in principle also be applicable to complex biological systems at interfaces which may involve enzymatic transformations or antigen–antibody interactions and where periodic order is present. Here we mention the elegant studies by Kornberg,[65] Ringsdorf,[66] and others, who monitored by electron-microscopic and fluorescence methods the dynamics of these interactions. We hope that deeper insight into some of these systems may be obtained by diffraction studies.

So far, most of the experiments had been carried out with "2D powders" at the smooth air–water interface. It is also possible to study the structure of thin organic films deposited on smooth solid supports.[78a] Recently, the structure of self-assembled monolayers on smooth mica coated with gold were determined in great detail.[78b] One may also anticipate, in the not too distant future, obtaining diffraction spectra from single crystals of these amphiphilic molecules and so providing structural information almost at the level of atomic resolution.

We thank Isabella Weissbuch, Ronit Popovitz-Biro, and Susan Weinbach for fruitful discussions. We acknowledge financial support from the German Israeli Foundation, the U.S.A.–Israel Binational Fundation, Jerusalem, the Petroleum Research Fund, the American Chemical Society, the Israel Academy of Sciences, the Danish Foundation for Natural Sciences, and HASYLAB, DESY, Hamburg, FRG for beam time.

Received: January 2, 1991 [A 851 IE]
German version: *Angew. Chem.* **1992**, *104*, 154

[1] I. Langmuir, *J. Am. Chem. Soc.* **1917**, *39*, 1848.
[2] J. D. Swalen, D. L. Allara, J. D. Andrade, E. A. Chandross, S. Garrof, J. Israelachvili, T. J. McCarthy, R. Munray, R. F. Pease, J. F. Rabolt, K. J. Wynne, H. Yu, *Langmuir* **1987**, *3*, 932.
[3] a) E. M. Landau, M. Levanon, L. Leiserowitz, M. Lahav, J. Sagiv, *Nature* **1985**, *318*, 353; b) E. M. Landau, S. Grayer Wolf, M. Levanon, L. Leiserowitz, M. Lahav, J. Sagiv, *J. Am. Chem. Soc.* **1989**, *111*, 1436; c) E. M. Landau, S. Grayer Wolf, J. Sagiv, M. Deutsch, K. Kjaer, J. Als-Nielsen, L. Leiserowitz, M. Lahav, *Pure Appl. Chem.* **1989**, *61*, 673; d) E. M. Landau, R. Popovitz-Biro, M. Levanon, L. Leiserowitz, M. Lahav, *Mol. Cryst. Liq. Cryst.* **1986**, *134*, 323; e) R. Popovitz-Biro, I. Weissbuch, D. Jacquemain, F. Leveiller, L. Leiserowitz, M. Lahav in *Advances in Industrial Crystallization* (Eds.: J. Garside, R. J. Davey, A. G. Jones), Butterworth-Heinemann, Oxford, **1991**, p. 3.
[4] a) S. Mann, B. R. Heywood, S. Rajam, J. D. Birchall, *Nature* **1988**, *334*, 692; b) S. Mann, *ibid.* **1988**, *332*, 119; c) S. Rajam, B. R. Heywood, J. B. A. Walker, S. Mann, R. J. Davey, J. D. Birchall, *J. Chem. Soc. Faraday Trans.* **1991**, *87*, 727; d) B. R. Heywood, S. Rajam, S. Mann, *ibid.* **1991**, *87*, 735; e) L. Addadi, J. Moradian, E. Shay, N. G. Maroudas, S. Weiner, *Proc. Natl. Acad. Sci. USA* **1987**, *84*, 2732.
[5] a) I. Weissbuch, L. Addadi, Z. Berkovitch-Yellin, E. Gati, M. Lahav, L. Leiserowitz, *Nature* **1984**, *310*, 161; b) I. Weissbuch, L. Addadi, L. Leiserowitz, M. Lahav, *J. Am. Chem. Soc.* **1988**, *110*, 561; c) I. Weissbuch, F. Frolow, L. Addadi, M. Lahav, L. Leiserowitz, *ibid.* **1990**, *112*, 7718.
[6] H. Kuhn, D. Möbius, *Angew. Chem.* **1971**, *83*, 672; *Angew. Chem. Int. Ed. Engl.* **1971**, *10*, 620.
[7] a) L. M. Blinov, N. V. Dubinin, L. V. Mikhnev, S. G. Yudin, *Thin Solid Films* **1984**, *120*, 161; b) T. Richardson, G. G. Roberts, M. E. C. Polywka, S. G. Davies, *ibid.* **1988**, *160*, 231; c) G. G. Roberts, B. Holcroft, A. Barraud, J. Richard, *ibid.* **1988**, *160*, 53.
[8] a) I. R. Girling, P. V. Kolinsky, N. A. Cade, J. D. Earls, I. R. Peterson, *Opt. Commun.* **1985**, *55*, 289; b) J. D. Swalen, *Thin Solid Films* **1988**, *160*, 197; c) W. Groh, D. Lupo, H. Sixl, *Angew. Chem. Adv. Mater.* **1989**, *101*, 1580; *Angew. Chem. Int. Ed. Engl. Adv. Mater.* **1989**, *28*, 1548; *Adv. Mater.* **1989**, 366; d) Y. R. Shen in *New Laser and Optical Investigations of Chemistry and Structure at Interfaces* (Eds.: R. B. Hall, A. B. Ellis), VCH, Weinheim, **1986**, p. 151; e) H. Fuchs, H. Ohst, W. Prass, *Adv. Mater.* **1991**, *3*, 10.
[9] a) G. G. Roberts, K. P. Paude, W. A. Barlow, *Proc. Inst. Electr. Eng.* **1978**, *125*, 169; b) T. Morizumi, *Thin Solid Films* **1988**, *160*, 413.
[10] G. Gaines, *Insoluble Monolayers at the Liquid-Gas Interface*, Interscience, New York, **1966**.
[11] a) T. F. Heinz, C. K. Chen, D. Ricard, Y. R. Shen, *Phys. Rev. Lett.* **1982**, *48*, 478; b) T. Rasing, Y. R. Shen, H. W. Kim, S. Grubb, *ibid.* **1985**, *55*, 2903; c) T. Rasing, G. Berkovic, Y. R. Shen, S. G. Grubb, M. W. Kim, *Chem. Phys. Lett.* **1986**, *130*, 1.
[12] a) D. L. Allara, R. G. Nuzzo, *Langmuir* **1985**, *1*, 52; b) J. Gun, R. Iscovici, J. Sagiv, *J. Colloid Interface Sci.* **1984**, *101*, 201.
[13] a) R. M. Weis, H. M. McConnell, *Nature* **1984**, *310*, 47; b) V. T. Moy, D. J. Keller, H. E. Graub, H. M. McConnell, *J. Phys. Chem.* **1986**, *90*, 3198; c) M. Lösche, E. Sachmann, H. Möhwald, *Ber. Bunsenges. Phys. Chem.* **1983**, *87*, 848; d) C. A. Helm, H. Möhwald, *J. Phys. Chem.* **1988**, *92*, 1262; e) C. M. Knobler, *Science* **1990**, *249*, 870.
[14] M. Lundquist, *Prog. Chem. Fats Other Lipids* **1978**, *16*, 101.
[15] R. W. James, *The Optical Principles of the Diffraction of X-Rays*, Ox Bow, Woodbridge, CT, USA, **1982**.
[16] M. Born, E. Wolf, *Principles of Optics*, MacMillan, New York, **1959**.
[17] a) W. C. Marra, P. Eisenberger, A. Y. Cho, *J. Appl. Phys.* **1979**, *50*, 6927; b) P. Eisenberger, W. C. Marra, *Phys. Rev. Lett.* **1981**, *46*, 1081.
[18] a) G. Vineyard, *Phys. Rev. B* **1982**, *26*, 4146; b) R. Feidenhans'l, *Surf. Sci. Rep.* **1989**, *10*, 105.
[19] J. Als-Nielsen, K. Kjaer, *NATO Adv. Study Inst. Ser., Ser. B* **1989**, *211*, 113.
[20] D. Jacquemain, S. Grayer Wolf, F. Leveiller, M. Lahav, L. Leiserowitz, M. Deutsch, K. Kjaer, J. Als-Nielsen, *J. Phys. Colloq.* **1989**, C7, p. 29.
[21] a) A. Braslau, M. Deutsch, P. S. Pershan, A. H. Weiss, J. Als-Nielsen, J. Bohr, *Phys. Rev. Lett.* **1985**, *54*, 114; b) A. Braslau, P. S. Pershan, G. Swislow, B. M. Ocko, J. Als-Nielsen, *Phys. Rev. A* **1988**, *38*, 2457; c) P. S. Pershan, *J. Phys. Colloq.* **1989**, C7, p. 1.
[22] a) J. M. Bloch, P. Eisenberger, *Nucl. Instrum. Methods Phys. Res. Sect. B* **1988**, *31*, 468; b) J. M. Bloch, *Phys. Rev. Lett.* **1988**, *61*, 2941.
[23] a) B. W. Batterman, *Phys. Rev.* **1964**, *133*, 1759; b) *Phys. Rev. Letts.* **1969**, *22*, 703.
[24] a) M. J. Bedzyk, D. H. Bilderback, G. M. Bommarito, M. Caffrey, J. S. Schildkraut, *Science* **1988**, *241*, 1788; b) M. J. Bedzyk, G. M. Bommarito, M. Caffrey, T. L. Penner, *ibid.* **1990**, *248*, 52; c) H. D. Abrunña, G. M. Bommarito, D. Acevedo, *ibid.* **1990**, *250*, 69; d) A. Ilda, T. Matsushita, T. Ishikawa, *Jpn. J. Appl. Phys.* **1985**, *24*, L 675; e) A. Y. Kazimirov, M. V. Kovalchuk, V. G. Kohn, Acta Crystallogr. Sect. A **1990**, *46*, 649.
[25] S. Grayer Wolf, L. Leiserowitz, M. Lahav, M. Deutsch, K. Kjaer, J. Als-Nielsen, *Nature* **1987**, *328*, 63.
[26] S. Grayer Wolf, M. Deutsch, E. M. Landau, M. Lahav, L. Leiserowitz, K. Kjaer, J. Als-Nielsen, *Science* **1988**, *242*, 1286.
[27] L. G. Parrat, *Phys. Rev.* **1954**, *95*, 359.
[28] K. Kjaer, J. Als-Nielsen, C. A. Helm, P. Tippman-Krayer, H. Möhwald, *J. Phys. Chem.* **1989**, *93*, 3200.
[29] A. Guinier, *X-Ray Diffraction*, Freeman, San Francisco, **1968**, Chap. 5.1.
[30] a) D. Jacquemain, S. Grayer Wolf, F. Leveiller, M. Lahav, L. Leiserowitz, M. Deutsch, K. Kjaer, J. Als-Nielsen, *J. Am. Chem. Soc.* **1990**, *112*, 7724; b) D. Jacquemain, unpublished.

[31] a) J. Als-Nielsen, F. Christensen, P. S. Pershan, *Phys. Rev. Lett.* **1982**, *48*, 1107; b) J. Als-Nielsen, P. S. Pershan, *Nucl. Instrum. Methods Phys. Res.* **1983**, *208*, 545.
[32] J. Als-Nielsen, H. Möhwald in *Handbook of Synchrotron Radiation Vol. IV* (Eds.: S. Ebashi, E. Rubenstein, M. Koch), North Holland, Amsterdam, in press.
[33] J. Als-Nielsen in *Handbook of Synchrotron Radiation Vol. III* (Eds.: S. Ebashi, E. Rubenstein, M. Koch), North Holland, Amsterdam, in press.
[34] J. M. Bloch, M. Sansome, F. Rondelez, D. G. Pfeiffer, P. Pincus, M. W. Kim, P. M. Eisenberger, *Phys. Rev. Lett.* **1985**, *54*, 1039.
[35] S. W. Barton, B. N. Thomas, E. B. Flom, S. Rice, B. Lin, J. B. Peng, J. B. Ketterson, P. Dutta, *J. Chem. Phys.* **1988**, *89*, 2257.
[36] Z. Berkovitch-Yellin, L. Leiserowitz, *J. Am. Chem. Soc.* **1982**, *104*, 4052.
[37] a) C. A. Helm, H. Möhwald, K. Kjaer, J. Als-Nielsen, *Biophys. J.* **1987**, *52*, 381; b) K. Kjaer, J. Als-Nielsen, C. A. Helm, L. A. Laxhuber, H. Möhwald, *Phys. Rev. Lett.* **1987**, *58*, 2224; c) C. A. Helm, H. Möhwald, K. Kjaer, J. Als-Nielsen, *Europhys. Lett.* **1987**, *4*, 697; d) P. Tippman-Krayer, C. A. Helm, H. Möhwald, J. Als-Nielsen, K. Kjaer, *Biophys. J.* **1991**, submitted.
[38] M. Elder, P. Hitchcock, R. Mason, G. G. Shipley, *Proc. R. Soc. London A* **1977**, *354*, 157.
[39] H.-P. Weber, R. K. McMullan, S. Swaminathan, B. M. Craven, *Acta Crystallogr. Sect. B* **1984**, *40*, 506.
[40] a) S. Grayer Wolf, E. M. Landau, M. Lahav, L. Leiserowitz, M. Deutsch, K. Kjaer, J. Als-Nielsen, *Thin Solid Films* **1988**, *159*, 29; b) S. Grayer Wolf, Ph.D. Thesis, The Weizmann Institute of Science, **1991**; c) S. Grayer Wolf, unpublished.
[41] B. Di Blasio, C. Pedone, A. Sirigu, *Acta Crystallogr. Sect. B* **1975**, *31*, 601.
[42] E. Benedetti, C. Pedone, A. Sirigu, *Acta Crystallogr. Sect. B* **1973**, *29*, 730.
[43] M. Mallikarjunan, S. Thyagarajarao, *Acta Crystallogr. Sect. B* **1969**, *25*, 296.
[44] M. S. Lehmann, T. F. Koetzle, W. C. Hamilton, *J. Am. Chem. Soc.* **1972**, *94*, 2657.
[45] J. Donohue, *J. Am. Chem. Soc.* **1950**, *72*, 949.
[46] T. M. Bohanon, B. Lin, M. C. Shish, G. E. Ice, P. Dutta, *Phys. Rev. B* **1990**, *41*, 4846.
[47] R. M. Kenn, C. Böhm, A. M. Bibo, I. R. Peterson, H. Möhwald, K. Kjaer, J. Als-Nielsen, *J. Phys. Chem.* **1991**, *95*, 2092.
[48] D. Jacquemain, F. Leveiller, S. P. Weinbach, M. Lahav, L. Leiserowitz, K. Kjaer, J. Als-Nielsen, *J. Am. Chem. Soc.* **1991**, *113*, 7684.
[49] a) S. Ställberg-Stenhagen, E. Stenhagen, *Nature* **1945**, *156*, 239; b) E. Stenhagen in *Determination of Organic Structures by Physical Methods* (Eds.: E. A. Braude, F. C. Nachod), Academic Press, New York, **1955**; c) A. M. Bibo, I. R. Peterson, *Adv. Mater.* **1990**, *2*, 309.
[50] B. Lin, M. C. Shih, T. M. Bohanon, G. E. Ice, P. Dutta, *Phys. Rev. Lett.* **1990**, *65*, 191.
[51] M. L. Schlossmann, D. K. Schwartz, P. S. Pershan, E. H. Kawamoto, G. J. Kellog, S. Lee, *Phys. Rev. Lett.* **1991**, *66*, 1599.
[52] D. M. Small, *The Physical Chemistry of Lipids, Handbook of Lipid Research Vol. 4*, Plenum, New York, **1986**.
[53] a) E. M. Lee, R. K. Thomas, J. Penfold, R. C. Ward, *J. Phys. Chem.* **1989**, *93*, 381; b) J. E. Bradley, E. M. Lee, R. K. Thomas, A. J. Willat, D. P. Gregory, J. Penfold, R. C. Ward, A. Waschkosky, *Langmuir* **1988**, *4*, 821.
[54] B. Berge, L. Faucheux, K. Schwab, A. Libehaber, *Nature* **1991**, *350*, 322.
[55] D. A. Dixon, F. A. van Catledge, B. E. Smart, *9th IUPAC Conf. Phys. Org. Chem.* **1988**, Abstr. p. A15.
[56] S. W. Barton, F. Rondeley, B. Lin, S. A. Rice, unpublished.
[57] a) J. D. Turner, E. C. Lingafelter, *Acta Crystallogr.* **1955**, *8*, 551; b) L. Leiserowitz, A. T. Hagler, *Proc. R. Soc. London A* **1983**, *388*, 133.
[58] a) R. M. Richardson, S. J. Roser, *Liq. Crysta.* **1987**, *2*, 797; b) M. J. Grundy, R. M. Richardson, S. J. Roser, J. Penfold, R. C. Ward, *Thin Solid Films* **1988**, *159*, 43; c) J. Daillant, L. Bosio, J. J. Benattar, J. Meunier, *Europhys. Lett.* **1989**, *8*, 453.
[59] P. Dutta, J. B. Peng, B. Lin, J. B. Ketterson, M. Prakash, *Phys. Rev. Lett.* **1987**, *58*, 2228.
[60] B. Di Blasio, V. Pavone, C. Pedone, *Cryst. Struct. Commun.* **1977**, *6*, 745.
[61] F. Leveiller, D. Jacquemain, M. Lahav, L. Leiserowitz, M. Deutsch, K. Kjaer, J. Als-Nielsen, *Science* **1991**, *252*, 1532.
[62] F. Leveiller et al., unpublished.
[63] M. Yazdanian, H. Yu, G. Zografi, *Langmuir* **1990**, *6*, 1093.
[64] B. Lin, T. M. Bohanon, M. C. Shih, P. Dutta, *Langmuir* **1990**, *6*, 1665.
[65] E. E. Uzgiris, R. D. Kornberg, *Nature* **1983**, *301*, 125.
[66] a) D. W. Grainger, A. Reichert, H. Ringsdorf, C. Salesse, *FEBS Lett.* **1989**, *252*, 73; b) M. Ahlers, R. Blankenburg, D. W. Grainger, H. Ringsdorf, C. Salesse, *Thin Solid Films* **1989**, *180*, 93; c) M. Ahlers, R. Blankenburg, H. Haas, D. Möbius, H. Möhwald, W. Müller, H. Ringsdorf, H.-U. Siegmund, *Adv. Mater.* **1991**, *3*, 39.
[67] I. Weissbuch, G. Berkovic, M. Lahav, L. Leiserowitz, *J. Am. Chem. Soc.* **1990**, *112*, 5874.
[68] M. Gavish, R. Popovitz-Biro, M. Lahav, L. Leiserowitz, *Science* **1990**, *250*, 973.
[69] S. Mann et al., unpublished.
[70] I. Weissbuch et al., unpublished.
[71] a) B. Vonnegut, *J. Appl. Phys.* **1947**, *18*, 593; b) M. L. Corrin, J. A. Nelson, *J. Phys. Chem.* **1968**, 643.
[72] a) R. C. Schnell, C. Vali, *Nature* **1972**, *263*, 163; b) L. R. Maki, E. L. Galyon, M. Chang Chien, D. R. Colwell, *Appl. Microbiol.* **1974**, *28*, 456; c) S. E. Lindow, D. C. Arny, C. D. Upper, *Phytopathology* **1978**, *68*, 523.
[73] N. Y. Fletcher, *The Chemical Physics of Ice*, Cambridge University Press, Cambridge, **1970**, p. 73.
[74] H. R. Prappacher, *Z. Angew. Math. Phys.* **1963**, *14*, 590.
[75] L. Pauling, *J. Am. Chem. Soc.* **1935**, *57*, 2680.
[76] I. Weissbuch, L. Leiserowitz, M. Lahav, *J. Am. Chem. Soc.* **1991**, *113*, 8491.
[77] H. D. Göbel, H. Möhwald, *Thin Solid Films* **1988**, *159*, 63.
[78] a) M. Seul, P. Eisenberger, H. M. McConnell, *Proc. Natl. Acad. Sci. USA* **1983**, *80*, 5795; b) M. G. Samant, C. A. Brown, J. G. Gordon, *Langmuir* **1991**, *7*, 437.
[79] B. Kamb, *Ice Polymorphism and the Structure of Water* (*Struct. Chem. Mol. Biol.* **1968**, 507).
[80] K. V. Titova, E. I. Kolmakova, V. Y. Rosolovskii, *Russ. J. Inorg. Chem. (Engl. Transl.)* **1982**, *27*, 347.